UNIVERSIDAD NACIONAL AUTÓNOMA DE MÉXICO

INSTITUTO DE ASTRONOMÍA
CENTRO DE RADIOASTRONOMÍA Y ASTROFÍSICA
INSTITUTO DE CIENCIAS NUCLEARES
FACULTAD DE CIENCIAS
DIVISIÓN DE ESTUDIOS DE POSGRADO

LA DISTRIBUCIÓN CENTRAL DE MATERIA
OBSCURA Y BARIÓNICA EN LA GALAXIA NGC
3367: UN ESTUDIO DETALLADO

T   E   S   I   S
QUE PARA OBTENER EL GRADO DE
MAESTRA   EN   CIENCIAS   (ASTRONOMÍA)
P   R   E   S   E   N   T   A:
FÍS.   MARIANA   CANO   DÍAZ

DIRECTORES DE TESIS:
DR. JOSÉ OCTAVIO VALENZUELA TIJERINO
DR. HÉCTOR MANUEL HERNÁNDEZ TOLEDO

instituto de astronomía
unam

CIUDAD UNIVERSITARIA, MÉXICO D.F.   2009

Agradecimientos:

A mi familia, en especial a mis padres y a mis abuelos por impulsarme en todos mis anhelos, personales y profesionales.

A todos mis amigos porque sin ellos mi vida estaría marchita.

A mis directores de tesis. Octavio por compartir conmigo siempre y con tanto entusiasmo su amplio conocimiento sobre Astronomía y Cómputo. Héctor por toda la dedicación que ha tenido en transmitirme su profundo conocimiento sobre Astronomía Observacional. Pero sobre todo les agradezco a ambos por impulsarme a continuar mi desarrollo en esta disciplina científica.

A los miembros de mi comité tutorial, por todos sus comentarios y recomendaciones. Vladimir Ávila Reese desde el comienzo de mi maestría y José Antonio García Barreto desde el comienzo de esta tesis (a quien en particular le agradezco por permitirme usar los datos en $H\alpha$ y en CO para NGC 3367 en esta tesis).

A Héctor Bravo Alfaro por permitirme analizar los datos en HI para NGC 3367 procesados por él.

A Jesús González González por sus excelentes comentarios que han ayudado a mejorar este proyecto.

A los miembros del jurado, por haber leído y revisado esta tesis.

Queriendo ver el océano inundé mis ojos de agua y de sal

queriendo sentir el viento extendí mis brazos y toqué la brisa del mar

pero queriendo vivir, miré hacia atrás y viendo a tantas personas dejé al mar y decidí regresar.

M.C.D.

Índice

1. Introducción

Estudios observacionales recientes concluyen que una fracción significativa (50-70%) de las galaxias espirales en el universo local tienen una estructura central en forma de barra (Hernández-Toledo et al. 2008, 2009; Menéndez-Delmestre et al. 2007; Barazza et al. 2009; Eskridge et al. 2000). El interés por estudiar el papel de éstas estructuras en la evolución galáctica es también creciente, debido a que está robustamente establecido en estudios dinámicos que éstas inducen redistribución de material y momento angular en las galaxias (Hohl 1978), alterando posiblemente las predicciones de los modelos de formación y evolución de galaxias para varias de las propiedades de discos y halos (Valenzuela & Klypin 2003; Debattista et al. 2004) . Además las estructuras de barra son observables a distancias y corrimientos al rojo considerables, lo que en principio permite utilizarlas como herramienta para estudiar la evolución de galaxias (Sheth et al. 2008). La redistribución de masa y momento angular causados por las barras galácticas, puede cambiar el contenido relativo de materia oscura y bariónica en el centro de las galaxias (Colín et al. 2006; Weinberg & Katz 2007; Sellwood 2008). Debido a esto el determinar dicho cociente de manera observacional es una prueba a los modelos de interacción dinámica entre bariones y la materia oscura. La teoría más simple y ampliamente utilizada, supone que durante la formación del disco bariónico el halo oscuro aumenta su densidad central o se comprime adiabáticamente (Blumenthal et al. 1986; Gnedin et al. 2004) . La existencia de las barras estelares sugiere que el efecto de contracción compite con el de la inyección de momento angular a través de las barras (Holley-Bockelmann et al. 2005) . Estudios como el propuesto en este trabajo ponen a prueba directamente este efecto.

El mapeo de la distribución de masa en galaxias espirales utilizando curvas de rotación es ya un ejercicio clásico en la astronomía, sin embargo no por ello carece de dificultades, en particular en los casos en que los discos galácticos muestran importantes perturbaciones,

y entre estas últimas está la existencia de barras centrales.

Existe una gran cantidad de estudios en los cuales se mapea la distribución de masa a través de la cinemática de galaxias axisimétricas (Rubin et al. 1978). En algunos trabajos se ha modelado ya la cinemática de galaxias espirales tomando en cuenta la contribución de la barra. En particular(Kalnajs & Athanassoula-Georgala 1974; Duval & Athanassoula 1983; Valenzuela et al. 2007; Spekkens & Sellwood 2007) muestran que el no tomar en cuenta este tipo de perturbaciones y trabajar bajo el supuesto de que todas las partículas de la galaxia se mueven en órbitas circulares, introduce errores considerables del orden de 30%- 50% en las restricciones para la estructura central de las galaxias. Por lo tanto es necesario tomar en cuenta las órbitas no circulares si se desean realizar estimaciones precisas. Sin embargo las caracterizaciones observacionales de los movimientos no circulares han consistido en medir simplemente la dispersión de velocidades perdiendo buena parte de la información sobre la naturaleza de las perturbaciones y asumiendo apriori que las desviaciones son una perturbación pequeña de la rotación. No existe además, una estrategia general para tomar en cuenta estas desviaciones de la rotación de manera simple. Estas limitantes pueden debilitar los intentos de restringir la estructura central de las galaxias y por lo mismo el poner a prueba predicciones de los modelos de formación de galaxias.

La tarea no es imposible sin embargo. En esta tesis se propone avanzar en esta dirección considerando toda la riqueza en la cinemática central de una galaxia que ha sido ampliamente estudiada con diferentes trazadores y en diferentes longitudes de onda. El esfuerzo por estudiar la estructura central de galaxias barradas a través de su cinemática, tiene precedentes. Entre los trabajos más recientes que buscan determinar el contenido y distribución de Materia Obscura en el centro de galaxias barradas, se encuentran: Weiner et al. (2001); Pérez et al. (2004), en el caso de galaxias externas y Bissantz et. al. (2003) en el caso de la Vía Láctea. Estos trabajos coinciden en concluir que no es necesaria la

materia oscura en el centro de estas galaxias. Estos resultados impicarían que la inyección de momento angular debido a la barra creó una expansión del halo de materia oscura, o que en su defecto no existe dicho componente. Sin embargo existen efectos sistemáticos en estos trabajos que nos hacen pensar que dicha afirmación es cuestionable y es por lo tanto, una de las motivaciones de esta tesis. De manera específica en los estudios mencionados anteriormente se considera solo la curva de rotación como una restricción a la distribución total de masa central. Dichos trabajos realizaron un estudio fotométrico y cinemático de galaxias barradas, posteriormente se realizaron simulaciones con potenciales barrados fijos o modelos semianalíticos para tratar de inferir la distribución de masa en el centro de las mismas, en todos ellos se hacen ciertas consideraciones para facilitar el estudio. Por ejemplo, Weiner et al. (2001) modelan el disco como un sistema en dos dimensiones, cuando justamente en la región central el espesor es comparable con el radio cilíndrico, se considera el papel de los choques pero no de los movimientos no-circualres. En el caso de Pérez et al. (2004), se utilizan observaciones de rendija larga para restringir la cinemática del disco. Dicha técnica sufre de una serie de efectos de proyección (Duval & Athanassoula 1983; Valenzuela et al. 2007; Spekkens & Sellwood 2007), por lo que es necesario contar con un mejor muestreo del campo de velocidades para restringir los modelos. Una etapa indispensable en los estudios previamente discutidos es la caracterización estructural y cinemática de las galaxias a analizar.

En esta tesis adoptamos estrategias similares pero la caracterización de la cinemática es mucho más completa ya que no promediamos la información solo en una curva de rotación. Nuestros modelos ajustan y disectan el campo de velocidades en diferentes componentes como rotación, movimiento radial, flujo bisimétrico (barra-disco elíptico) o fuera de centro (lopsidedness). Esto permite dar un diagnóstico del estado dinámico de la galaxia. En nuestro conocimiento es la primera vez que se utiliza esta técnica para dicho tipo de estudio. El análisis se realizó gracias al software VELFIT, el cuál se desarrolla actualmente por

Kristine Spekkens (RMC, Canada), este estudio de hecho contribuye a poner a prueba las capacidades de dicho software. Es importante advertir que a pesar de la flexibilidad del modelo utilizado para interpretar a las observaciones, este tiene limitantes como todo modelo. En particular, no se considera un caso en que todos los posibles componentes cinemáticos mencionados anteriormente se superpongan. La principal razón para esto, se debe a que las separación del campo de velocidades observado en tanta componentes, reduce la señal a ruido para cada uno de éstas contribuciones, básicamente la misma señal se divide pero el ruido permanece constante. Esto puede afectar de manera grave el ajuste multiparamétrico necesario para asignar una interpretación para el campo de velocidades, y hacerlo sensible principalmente a las propiedades del ruido. Como una alternativa a este problema decidimos aislar zonas en las que las propiedades geométricas del campo de velocidades son homogeneas, como la parte central o más externa y ajustarles un modelo, además de construir modelos a todo el mapa cinemático, esto pone también a prueba la autoconsistencia de nuestra interpretación de las observaciones.

El llamado artículo I Hernández-Toledo et al. (2009), está enfocado en la fotometría y caracterización de la estructura de la galaxia, en particular sus asimetrías, así como las propiedades de la barra. El artículo se presenta como un apéndice, dada la longitud del mismo y la división de tareas entre los diferentes autores. En el artículo central de ésta tesis, se presenta un breve resumen y un análisis nuevo. En particular, se caracteriza la contribución del disco a la velocidad circular a través del campo de fuerzas utilizado en el artículo I para estimar la fuerza de la barra. Este campo se obtuvo resolviendo la ecuación de poisson a partir de un mapa de brillo superficial y un coeficiente de conversión masa luminosidad estelar, esta estrategia permite relajar una serie de suposiciones geométricas comunmente presentes en los análisis bulbo-barra-disco. Se decidió utilizar una M/L estelar unitaria y constante, sin embargo utilizando mapas de color como los mostrados es posible incluir incluso la presencia de gradientes de población estelar. Esta novedosa estrategia se

explotará en un estudio posterior con el objetivo de estimar lo más precisamente posible la abundancia de diferentes componentes en la estructura central de NGC 3367.

Los resultados presentados en esta tesis, se obtuvieron de la reducción y análisis de observaciones fotométricas (Bandas BVRIJHK, Observatorio Astronómico Nacional, San Pedro Mártir, Baja California, México. 3.6, 4.5 y 5.8 μm, Spitzer Space Telescope) y cinemáticas ($H\alpha$, interferómetro Fabry-Perot PUMA, Observatorio Astronómico Nacional, San Pedro Mártir, Baja California, México, HI, interferómetro VLA y CO, interferómetro OVRAM) de la galaxia aislada espiral barrada NGC3367. En todos los casos se obtuvo el cubo de datos calibrado en velocidades, la mayor parte del trabajo constitió en crear los campos de velocidades, así como modelar dichos campos con el fin de determinar tanto la geometría del disco como restringir su estado dinámico. En el caso particular del H-α se aplicó un procedimiento para enfatizar las estructuras de alta señal a ruido suavizando las observaciones con un kernel gausiano con un tamaño de ventana variable.

2. Article

Central Dark and Baryonic Mass Distribution in Barred Galaxies:

NGC 3367 Kinematics

M. Cano-Díaz[1,a] O. Valenzuela[1] H. M. Hernández-Toledo[1] J. A. García-Barreto[1] H. Bravo-Alfaro[3] K. Spekkens[2]

2.1. Abstract

It is well established that streaming motions in barred galaxies are useful to break the disk-halo degeneracy. Here we present the results of a multi-wavelength photometric (optical, NIR, MIR) and kinematic ($H\alpha$, HI and CO) analysis of the isolated Seyfert barred galaxy NGC 3367. Using the radial force field calculated in paper I, solving the Poisson equation based on the 3.6 μ surface brightness distribution, we calculated the disk/bar/bulge circular velocity contribution at every pixel. We dissect the velocity fields into rotational velocity and different non-circular components of motion (bi-symmetric, lopsidedness, radial). We also characterized the shape and velocity jumps related to shocks in the bar region. The $B - R$ color map reveals a prominent curved dust lane which is a constraint to the geometry of ISM bar induced shocks. We found that regardless of a tilted ring analysis with variable inclination the asymmetry in the HI rotation curve is preserved, making less appealing the warp explanation for the asymmetries. The HI and the H-α kinematics can be explained by a kinematically lopsided model, however the amplitude and sign of the m=1 kinematic perturbation is unphysically large, suggesting that lopsidedness is likely the effect of extraplanar gas along the line of sight in the NE region. We found that a by-symmetric model is the most reasonable representation of the velocity field for the central region 4 kpc. The CO velocity field presents considerable random motions, however

a rotation and by-symmetric pattern is consistent with the H-α and CO kinematics. We conclude that besides the apparent lopsidedness in the stellar component and the large scale kinematics, NGC 3367 is suitable of dynamical studies. The large scale asymmetries are likely the result of extraplanar gas, coming from accretion or a large scale tidal bridge. These results will be used in a forthcoming paper where a dynamical interpretation will set constraints on the amount of dark and visible matter in the central region of NGC 3367. If the accretion model is confirmed by future high sensitivity HI studies, a possible connection between AGN activity and cosmic gas accretion is suggested.

2.2. Introduction

Observational studies show that an important fraction of spiral galaxies in the local universe (40-70%) are barred (Eskridge et al. 2000; Menéndez-Delmestre et al. 2007; Barazza et al. 2009; Hernández-Toledo et al. 2008, 2009). This fact has stimulated studies about the role of bar dynamics in galaxy evolution. Recently the bar-dark matter halo dynamical interaction has captured special interest because it might change predictions for the structure of galaxies based on dark matter only cosmological simulations (Valenzuela & Klypin 2003; Debattista et al. 2004). A specially interesting aspect is the relative amount of dark and visible matter in the central region of galaxies where a bar is present (inside an exponential scale radius). This quantity is presumably sensitive to the exchange of angular momentum between baryons and the dark matter halo (Colín et al. 2006; Weinberg & Katz 2007; Sellwood 2008). However, its observational estimation is not a well determined problem usually known as the disk-halo degeneracy. The internal galaxy kinematics in barred galaxies is an important element to break the mentioned degeneracy, because the bar triggered non-circular motions and shocks depend on the bar pattern speed, shape and mass. If we are able to calibrate these properties it is possible to constrain the disk

stellar M/L independently of stellar population models. In order to do that, independent measurements of shock geometry, velocity jumps and bar photometry are used. This promissory technique has already been applied to some galaxies. However, previous theoretical and observational studies show contradictory results when investigating the disk-halo degeneracy in the central region of barred spiral galaxies. Weiner et al. (2001b) and Weiner et al. (2001) made a study of the disk-halo degeneracy problem in the galaxy NGC 4123, making use of the bar induced gas streaming motions and shocks mapped in the $H\alpha$ line to constrain the stellar disk M/L ratio independently of stellar population models and HI observations to fix the global mass. They compared the observations with galaxy simulations fitting parameters like the mass-luminosity (M/L) ratio and the bar pattern speed, and concluding that NGC 4123 is dominated by luminous matter in the disk and that the bar is a fast rotator. Pérez et al. (2004) ran Smooth Particle Hydrodynamics (SPH) simulations of five barred galaxies, using the rigid potentials derived from NIR light distribution observations, in order to reproduce the $H\alpha$ (long slit observations) rotation curves as well as the disk gaseous morphology. A dark matter halo component was included only for two of the five galaxies. The study concluded that the best fit was the one with no dark matter halo component. An important aspect not considered in the previous analysis is the modeling of non-circular motions, instead a cylindrically averaged rotation curve built from the average of slits observations with different position angles is used as a constraint. This simplification was probably motivated by the assumption that non-circular motions are small perturbations to rotation, however this is not likely the case in a barred galaxy (Kalnajs & Athanassoula-Georgala 1974; Duval & Athanassoula 1983; Rhee et al. 2004; Valenzuela et al. 2007; Spekkens & Sellwood 2007) , questioning their conclusions about the lack of need for dark matter. In contrast, theoretical models about the dark matter halo response to the baryonic galaxy formation, dubbed as adiabatic compression (Blumenthal et al. 1986; Gnedin et al. 2004) predict a comparable amount of dark matter and baryons.

Therefore more investigation of this situation is needed, from both, observational and theoretical sides. The main goal is to either verify the dearth of dark matter in the bar region of disk galaxies or alternatively update adiabatic contraction models. Noteworthy, NGC3367 is a Seyfert galaxy, showing a radio continuum jet. It is by itself interesting to constrain the mass distribution surrounding the blackhole at scales of hundreds of parsecs, looking for evidence of joint dynamical evolution.

This is the second of a series of papers devoted to determine the baryonic and dark mass in the central region of barred spiral galaxies. We focus now in the galaxy NGC 3367 kinematics. In order to apply the ideas discussed in Weiner et al. (2001), we model the non-circular motions using a Fourier decomposition scheme suggested by Spekkens & Sellwood (2007), that avoids the epicyclic approximation. In particular we study bar related projection effects and its kinematic signature using bi-symmetric terms, but also the lopsidedness features, as well as a model with radial expansion. It is well known that omitting bi-symmetric corrections introduce important biases to the interpretation of rotation curves (e.g. Duval & Athanassoula, Rhee et al. 2004, Valenzuela et al. 2007). The disk geometry (inclination and PA) is one of the important uncertainties. One of our study novelties lies on using different kinematic tracers like $H\alpha$, HI and CO and their corresponding kinematic dissection. In this paper we focus on the construction of the kinematic map for NGC 3367, favoring high signal to noise ratio features. However we present here a basic interpretation in terms of rotation curves. We will use these results in a forthcoming paper to distinguish models of the central matter structure, particularly of the dark and baryonic matter in the central region of the galaxy.

The content of this paper is as follows: Section 2 describes the observations used in this study, section 3 summarizes the methods behind the analysis of the velocity fields. In section 4 we show our results, and in sections 5 and 6 we present our discussion and

conclusions respectively.

2.3. NGC3367: General Properties

2.3.1. Basic Properties

NGC3367 is a nearby barred spiral galaxy classified as SB(rs)c (NED/Leda) (see figure 1). It has a B-band magnitude $B = 12.05$, and the spectra from its central region suggests that it is an active galaxy of the Sy-like/HII type (Veron-Cetty & Veron 1986; Ho et al. 1997). At a distance of $43.6Mpc$, $1''$ corresponds to $210pc$. This galaxy lies behind the Leo group of galaxies (García-Barreto et al. 2007). Its closest companion is located at a projected distance of $\approx 563kpc$ (18 optical diameters away) (García-Barreto et al. 2003) indicating that it is an isolated galaxy.

NGC 3367 has an inclination of $\sim 30°$ (García-Barreto & Rosado 2001). The stellar bar has a length of $\approx 32'' \sim 6.7kpc$ with a $P.A$ of $\approx 65°$ - $70°$.

NGC 3367 shows thermal continuum emission through the disk as well as bipolar synchrotron outflow and two lobes with a total extent on the sky from the nucleus of $\approx 12kpc$ (García-Barreto et al. 1998). This galaxy has a high molecular gas content, mostly concentrated in the central region $9''$ with an unresolved source (García-Barreto et al. 2005).

The closeness and brightness of this galaxy allow us to obtain high quality/resolution observations in several tracers, and hence to study in detail the kinematics signatures of its components like the bar. NGC 3367 is an isolated barred galaxy and we will consider it as representative of this galaxy population.
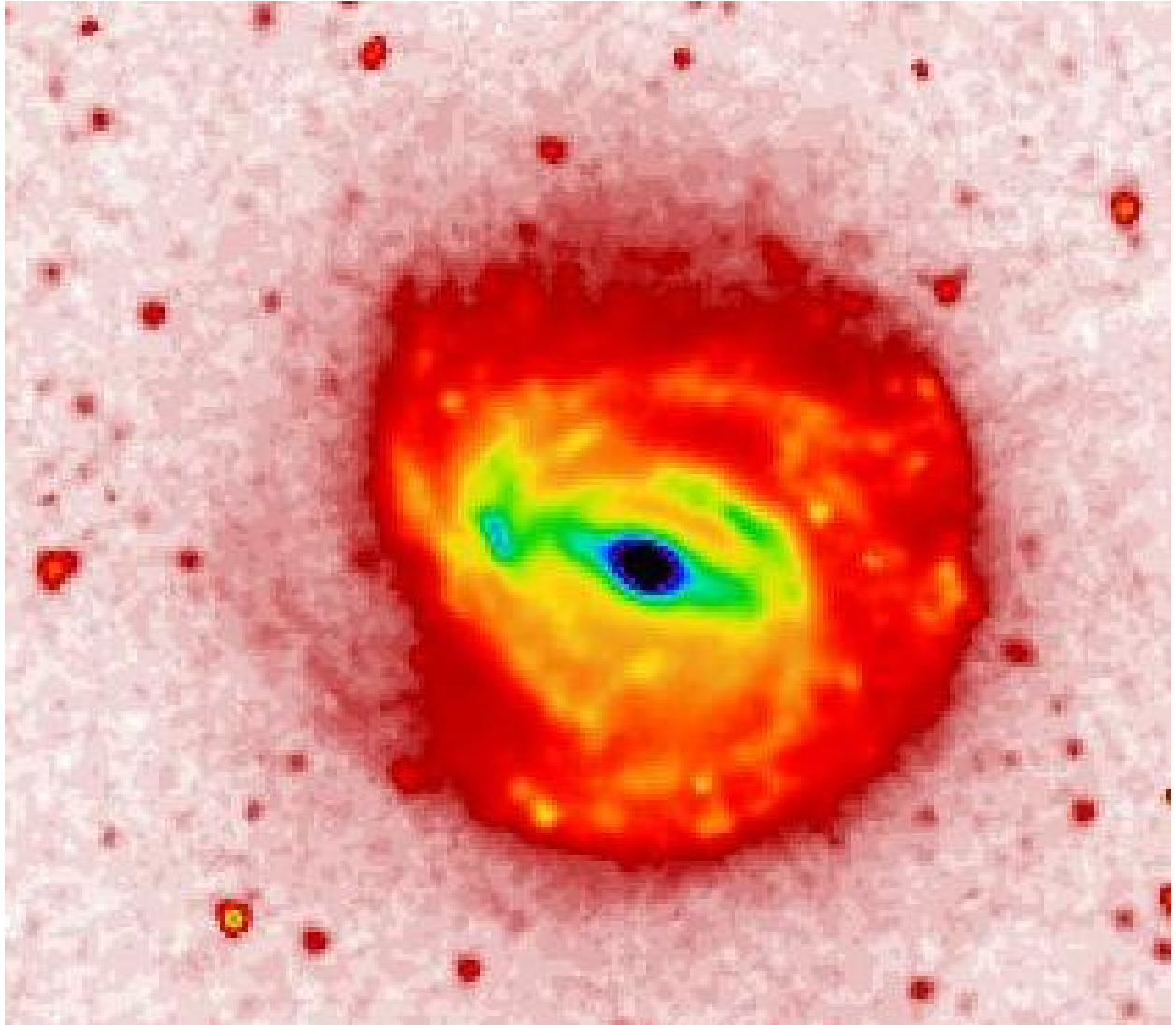
Fig. 1.— NGC 3367 image in 3.6μ (Spitzer Space Telescope).

2.4. Surface Photometry

Although we are going to present a simple interpretation of the galaxy kinematics, a detailed information of the surface photometry is necessary in order to constraint the galaxy structural and geometrical parameters. An extensive analysis was already presented by (Hernández-Toledo et al. 2009), here we present only the basic information for the sake of completeness. (See Fig. 2).

We use broad-band BVRIJHK (Observatorio Astronómico Nacional, San Pedro Mártir, Baja California, México) as well as 3.6 μm (Spitzer Space Telescope) photometric study (Hernandez-Toledo et al (submitted)). For further information see Sections 5 and 6. The kinematic analysis makes use of the ellipticity, disk and bar position angle.
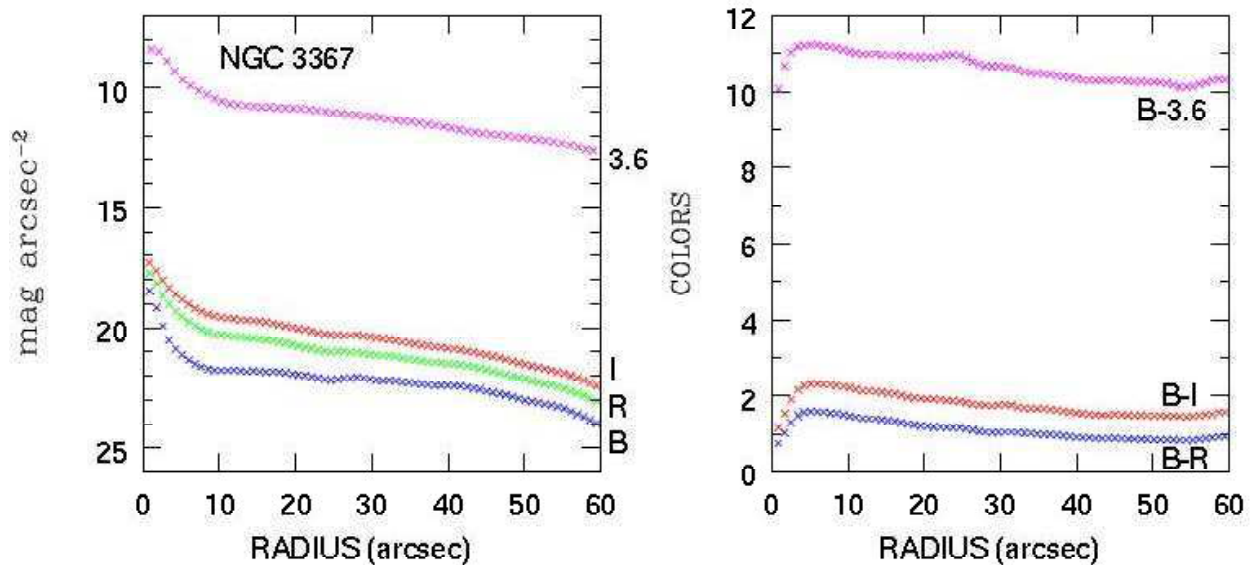

Fig. 2.— Surface Brightness profiles for the B, R, I and 3.6 μm bands as well as their correspondent color profiles

The Hernández-Toledo et al. (2009) photometric study provided us the first constraints

on the bar nature. Among these are the dust lane geometry, using a $B - I$ color map of NGC 3367 (Fig. 3). Dust lanes are formed due to gas shocks. The observed dust lane curved shape in NGC 3367 suggests that the bar might not be a fast rotator according to the results by Athanassoula (1992). However the constraint is degenerated, because the bar strength, stellar mass to light ratio and the ISM effective equation of state play also a role defining the shock geometry. We measured the bar strength using the estimator introduced by Buta & Block (2001) and using k-band observations. In order to break degeneracies it is also important to directly measure the bar pattern speed. Previous studies let this quantity as a free parameter (Weiner et al. 2001). Previous Bar pattern speed estimation of NGC 3367 are given by García-Barreto & Rosado (2001) and Gabbasov et al. (2009). The last authors followed the Tremaine & Weinberg (1984) method based on the continuity equation for a gaseous tracer ($H\alpha$) and obtained 43 km/s/kpc $\pm$ 6. Applying the TW method using gaseous tracers is still a controversial technique that it is important to verify using stellar kinematics. We this aim we performed spectroscopic observations for the stellar component in NGC3367. Results will be published soon as a part of this series of papers (Cano et al. 2010 in preparation).
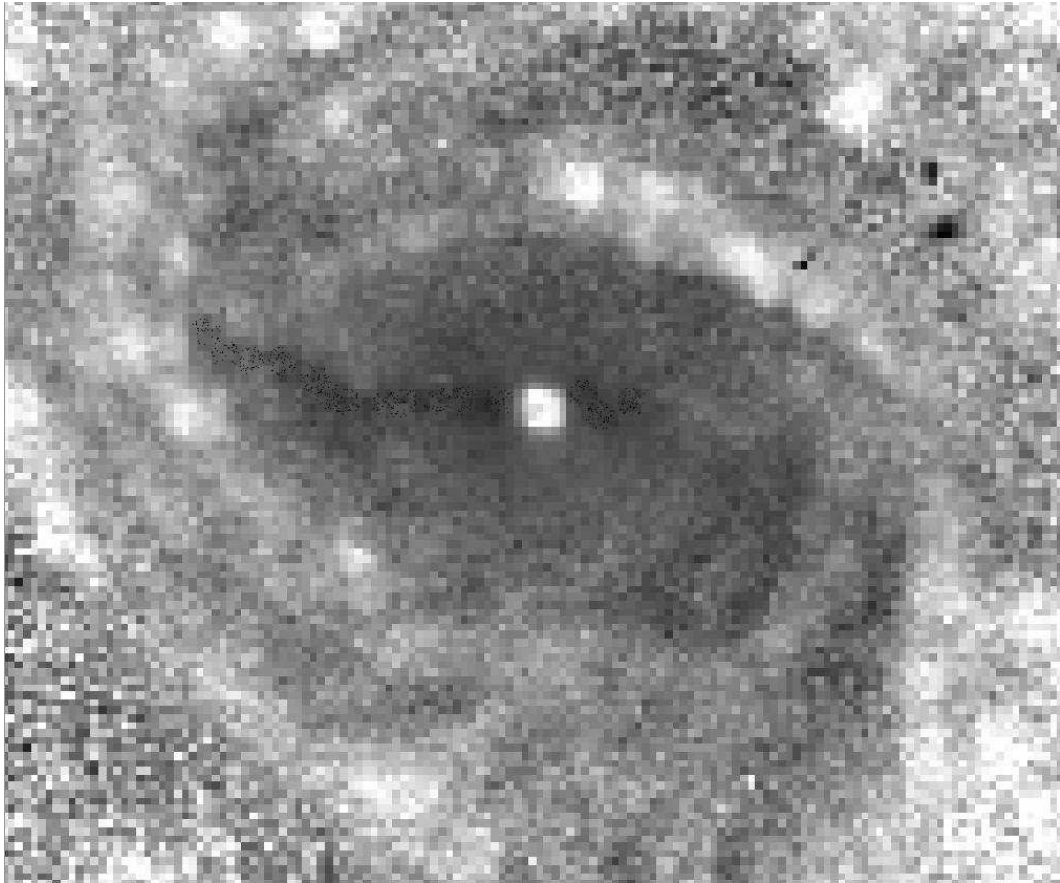
Fig. 3.— Inner region of the $B - I$ color map of NGC 3367. Darker colors are redder. The dust lane in the bar is apparent as a dark line running mainly at the east of the nucleus. The nucleus and the arms are bluer.

2.4.1. Disk Structure and Circular Velocity

We use the 3.6 microns surface brightness observations in order to estimate the disk contribution to the circular velocity. The procedure has been previously explained in (Buta & Block 2001; Hernández-Toledo et al. 2009) . Here we just briefly describe the procedure. First we de-project the galaxy, and spread the surface brightness in a grid. Next we use the grid and an unitary stellar M/L in order to have a density distribution and solve the Poisson equation. Lastly we derive the potential in each cell (Fig. 4) , in order to calculate the radial force. The usual procedure is to use the galaxy luminosity and color combined with stellar population models in order to estimated the disk total mass. However, the AGN presence in NGC3367 biases this strategy. We normalized the disk maximum circular velocity using an empirical relationship between the disk exponential scale and thickness proposed by Bottema (.Bottema (1993)) It is important to mention that we decided not to use a photometric method because the presence of an AGN biases the estimation of luminosity and mass. The calibration we use assumes a maximum disk, therefore our estimation is an upper limit to the disk circular velocity. Note that this estimation is potentially free from geometrical assumptions to the disk/bar/bulge components and is able to capture possible gradients in the stellar population (M/L ratio) minimizing systematic effects in the central mass distribution studies in galaxies. We will fully exploit this benefits in a forthcoming study. We multiply the radial force times the galactocentric distance in order to estimate the square of circular velocity in each pixel (Fig. 5). We end up with a 2D map of disk circular velocities. We average this quantity in order to get a profile and do a preliminary analysis of rotation curves in this paper. The full map will be used in a more detailed future study.
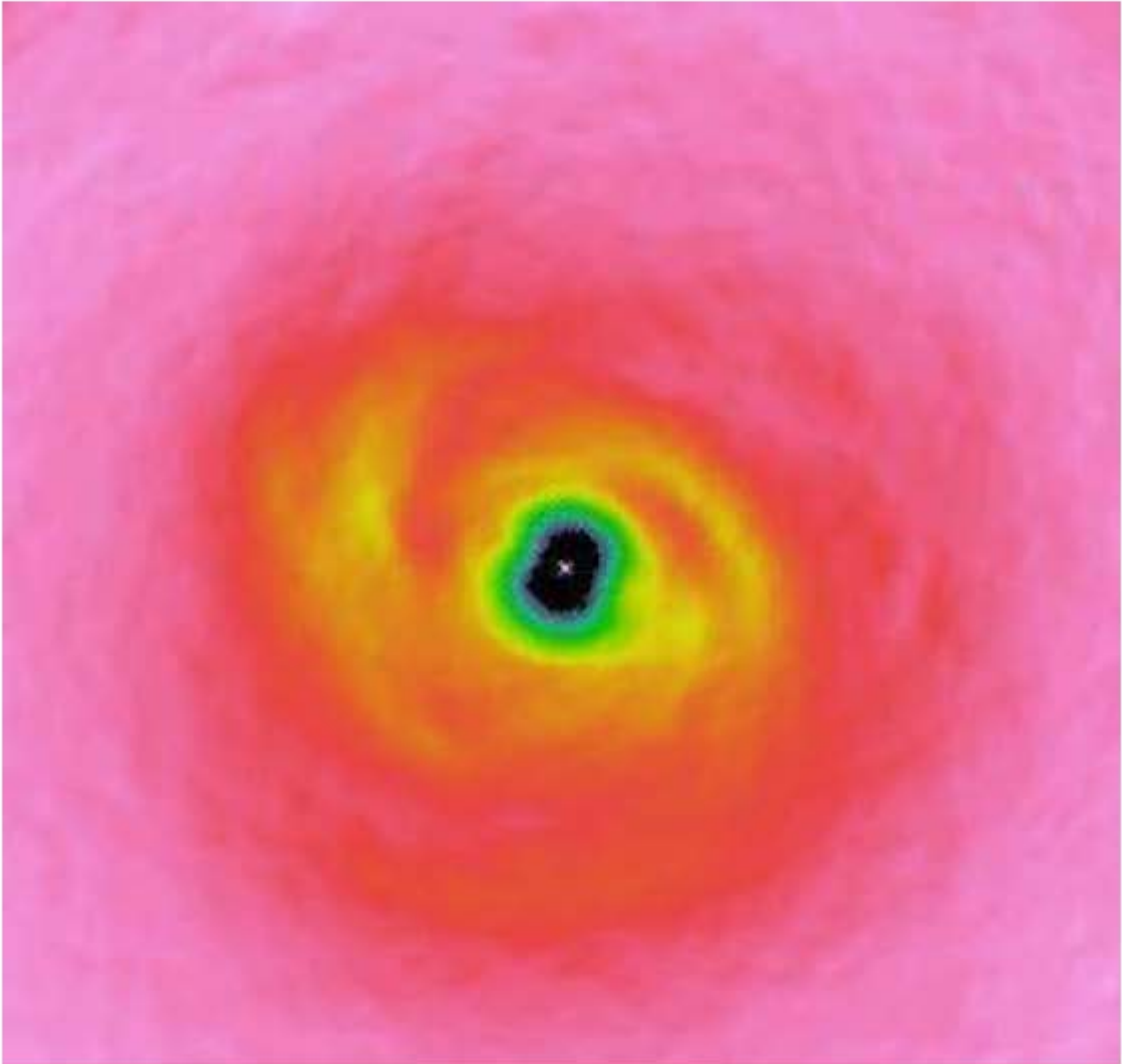
Fig. 4.— 3.6μm radial force map. The region that encloses the spiral arms corresponds to 83 *arcsec*. The ratio between maximum and minimum pixel values is 1.36

Fig. 5.— 3.6μm Circular velocity map. The region that enclose the spiral arms of the galaxy corresponds to 83 *arcsec*. The ratio between maximum and minimum pixel values is 1.4, when 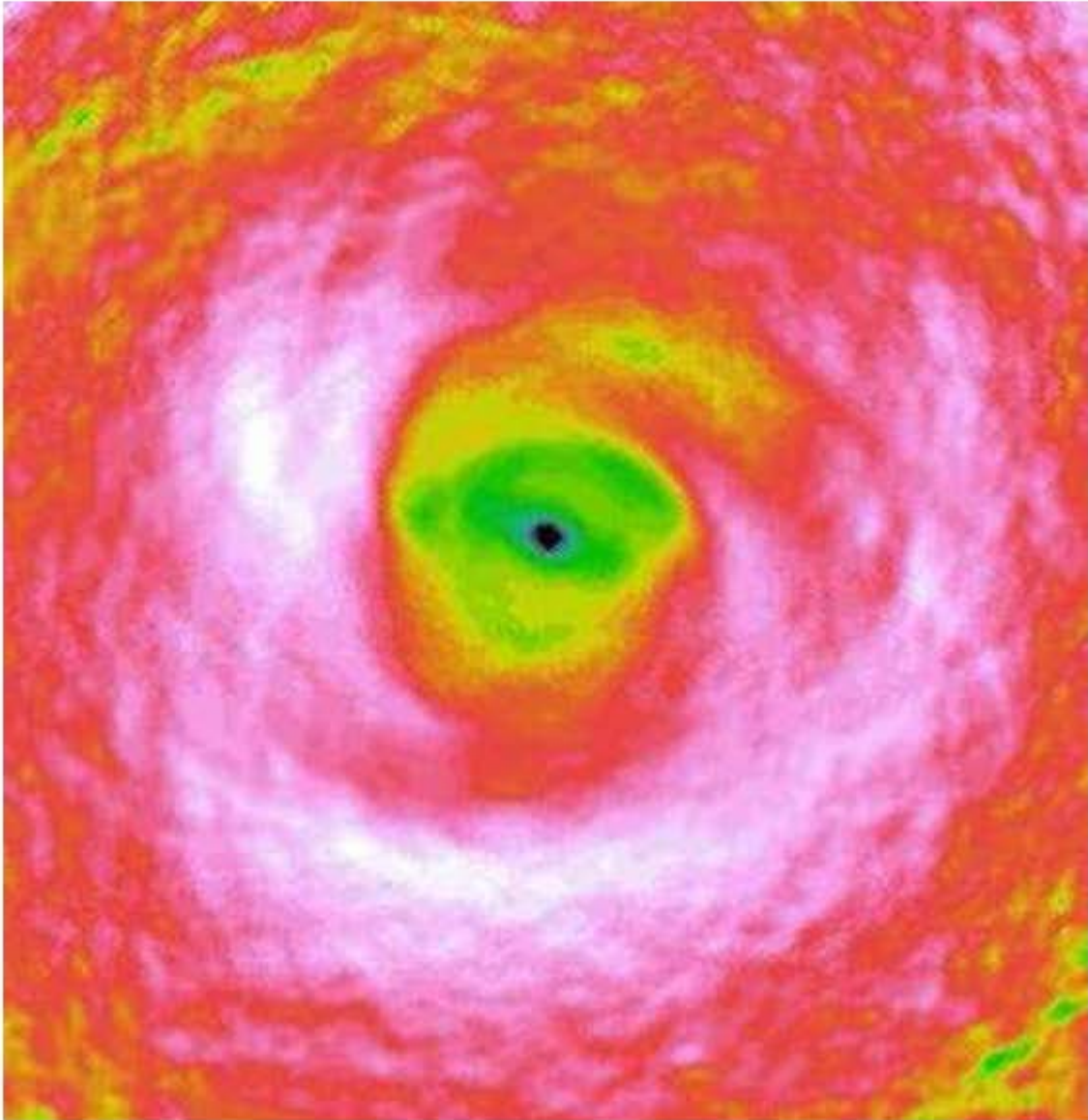using a Botema disk (Bottema (1993)) assuming a 500 pc (300 *pc*) height the maximum value corresponds to $140km/s$ ($180km/s$) (See text discussion).In this image it es very noticeable an asymmetry between the north and south sides of this field.

2.5. Kinematic Data

As we already stated in the introduction, one of the novelties of our work is to use several tracers for the study of NGC 3367 galaxy kinematics. $H\alpha$, HI, and CO tracers are spatially complementary, we will see in the following subsections that none of the tracers map every single part of the galaxy. Each tracer velocity field have zones where the signal to noise (S/N) ratio is extremely low, or just there is no signal at all. Lastly, the possible systematic effects affecting each tracer are different, therefore we can seek for an internal consistency test of our results.

2.5.1. Hα Fabry-Perot Data and Reduction

The H-α observations were performed with the Fabry-Perot PUMA at the 2.1 meter telescope at the Observatorio Astronómico Nacional, San Pedro Mártir, Baja California, México. The velocity field has already been published (García-Barreto & Rosado 2001).

The Fabry Perot interferometer setup is described in (García-Barreto & Rosado 2001). For our study we performed again some steps of the basic calibration in order to re-estimate the velocity field. First cosmic rays were eliminated by using corrective IRAF routines. The next step was setting all of the channels at the same resolution. We measured the FWHM of a reference star, then all the images were set to the same resolution by using the kernel in the GAUSS IRAF routine, using a window size consistent with the lowest resolution channel. Finally it was necessary to recenter all the images to a common reference position.

After that, the AIPS software was used to obtain the three moments of the data cube, related to intensity, velocity field and velocity dispersion. We did not subtracted any sky lines because the redshifted emission range of the galaxy lies between 6619 and 6629 $\mathring{A}$, excluding the presence of strong sky lines in this range.

In figure (upper right panel of the Fig. 6) we show the $H\alpha$ velocity field. It is easily to note that there are regions where there is no signal, specially in the left side of the galaxy.

2.5.2. $H\alpha$ Data smoothing

$H\alpha$ emission data from galaxies often present a low signal to noise ratio (S/N) when it is embedded in a diffuse area, in spite of long integration times. There are techniques that help to improve the S/N in an image, or at least to make it homogeneous. These procedures are usually a trade-off between angular resolution and S/N. With that purpose we implemented a spatial smoothing technique that uses a variable kernel. The kernel was designed to smooth every image pixel to a desired S/N (Daigle et al. 2006), our goal was to enhance high S/N features and to smooth out velocity structures which are likely the outcome of noise, but that can bias the multiparametric fit to the velocity field. The first performed step was to estimate the S/N in each pixel. That computation was done by the following equation:

$$S/N = \frac{x_i}{\sqrt{x_i + \sigma^2}}. \tag{2.5.1}$$

Where x_i is the intensity of the i-th pixel and σ is the dispersion of each pixel spectrum. The estimation of σ was done measuring the dispersion of the spectrum in different pixels as suggested by Daigle et al. (2006).

With this estimation we applied a variable Gaussian kernel (Merritt & Tremblay 1994) given by the following equations:

$$\widehat{f_k(x)} = \frac{1}{nh} \sum_{i=1}^{n} K(\frac{x - X_i}{h}), \tag{2.5.2}$$

where $\widehat{f_k(x)}$ is the kernel estimator of a normalized function $f(x)$, evaluated in the x pixel with respect of the rest X_i pixels of the image. n is the total number of pixels and h is called the window width or smoothing parameter. As stated above, we decided to use a Gaussian kernel:

$$K(y) = \frac{1}{\sqrt{2\pi}} e^{-y^2/2} \qquad (2.5.3)$$

In our image smoothing process we let h vary for every pixel until a desirable S/N is reached. Once the kernel estimator is computed for every pixel of the image with an individual h value a smoothed velocity field is obtained.

2.5.3. HI and CO data

We also have HI data, acquired with the Very Large Array (VLA). The HI data cube was obtained with the C VLA configuration in the year 2001, and it is divided in 63 spectral channels with a spectral resolution of $11km/s$ (half channel width, private communication H. Bravo-Alfaro) The basic reduction was performed by H. Bravo-Alfaro (2010 in preparation). We also have available CO observations, obtained with the Owens Valley Millimeter Array in four antenna configurations (C, L, E iand H) in 2003. With an spectral resolution of $5km/s$ (García-Barreto et al. (2005)). The data reduction analysis needed to obtain the velocity field has been discussed in the last same reference.

In particular for the HI and CO tracers. it is easy to note how well they complement each other. By looking at the HI velocity field we will note that emission is absent in the central region resembling a large scale toroidal shape, where the external radius is of $80''$, and the internal radius is of $20''$. Meanwhile the CO emission (with a radius of $28''$) is enclosed by the inner region of the HI torus. Notice that by combining the HI, CO and

$H\alpha$ data we will have more kinematic information at the bar region, where noncircular motions are produced. Detailed analysis of noncircular motions are of particular interest to our study.

In the upper right panel of Fig. 12 we show the HI velocity field, where the toroidal shape is easily recognizable. Also we can notice that in the HI torus we have a very smooth emission.

In figure (Fig. 10) we show the CO velocity field.

2.6. Velocity field analysis

2.6.1. Tilted ring model

The tilted ring model is a standard procedure to model spiral galaxy kinematics (Begeman 1989). In this model a galaxy is described as a set of concentric rings. Each of them has a characteristic surface density, circular velocity V_c, inclination angle i and position angle of mayor axis ϕ. Also the whole system is described by the systemic velocity V_0 and center coordinates x_o, y_o. For an axi-symmetric galaxy the rings geometry can be fixed using the surface brightness, and the other three are determined by an iterative procedure. The rings model can be set to a specific systemic velocity value or this could be also considered as a free parameter. The situation is not fully determined if the galaxy is not axi-symmetric. Extensions to the standard tilted ring analysis have been suggested, these improvements make use of relationships between non-circular motions and the true shape of the potential, however they are mostly based on the epicyclic approximation making them less suited for strong perturbations like barred potentials. Nevertheless, we will initially make an axi-symmetric tilted analysis, focused to the external region of the galaxy where the bar perturbation is expected to be less important. As a comparison

we will also apply the axisymmetric analysis to the bar region, however a more general modeling will be presented in section 2.6.2

In order to get a robust solution, this model needs at least 30 points per each ring. It is also important to note that this model is not reliable to explain the kinematic behavior in the central parts of a galaxy, because the velocity gradients in this regions are too high to be well described with a simple rings model. It is also desirable to have galaxies with inclination angles (i) ranging between 50 and 80 degrees.

For each ring, the velocity in the plane of the sky-coordinates is characterized by the following equations:

$$V(x,y) = V_o + V_c(R)\sin(i)\cos(\theta) \tag{2.6.1}$$

$$\cos(\theta) = \frac{-(x-x_0)\sin(\theta) + (y-y_0)\cos(\theta)}{R} \tag{2.6.2}$$

$$\sin(\theta) = \frac{-(x-x_0)\cos(\theta) - (y-y_0)\sin(\theta)}{R\cos(i)} \tag{2.6.3}$$

In order to fix the geometry of each annulus a fit to the desired parameters $(V_0, x_0, y_0, V_c, i, \phi)$ is carried out by using the observed velocity in each point (velocity field), as well as an initial guess of the parameters, and by performing an iterative process we are able to get the best set of values by determining the minimum χ^2 solution.

We decided to apply this modeling procedure to the HI velocity field, because the emission extends only to the outer parts of the galaxy, where we expect that the non axisymmetric potential of the bar do not affect much the kinematics of this region, allowing us to apply this method that do not model non-circular motions in order to restrict the

geometric parameters (such as inclination i, position angle $P.A.$, center and systemic velocity) at least in the outer parts of the galaxy.

2.6.2. Non Circular Motions Modeling

In order to perform a more general modeling of the velocity field we used the method provided by Spekkens & Sellwood (2007). In this method the authors make a Fourier mode decomposition of the velocity field, they focused on the bi-symmetric mode (m=2) and a radial flow for the galaxy NGC 2976. Their analysis is supported under four main hypotheses. First, that the non-circular motions are due to a non-axisymmetric perturbation such as a prolate dark matter halo or the presence of a bar in the barionic mass distribution. Second that the observed velocity in this type of potentials could be well represented as a finite Fourier series:

$$V_{model} = V_{sys} + \sin(i) \left[\ \overline{V_t} \cos\theta - V_{m,t} \cos(m\theta_b) \cos(\theta) - V_{m,r} \sin(m\theta_b \sin(\theta)) \ \right] \qquad (2.6.4)$$

(θ is the position angle of a disk pixel, i the inclination angle, V_t the tangential velocity component in the disk reference frame, V_r the radial velocity component and m the harmonic order. Spekkens & Sellwood (2007) chose as a maximum $m = 2$, as this mode corresponds to the bar geometry, because a bar rotating $\frac{360°}{m=2} = 180°$, returns it to its original position, while $m = 1$ correspond to a lopsided perturbation. Their third hypothesis is that the flow along the observer line of sight over the bar mayor axis is the lowest, while, the one over the bar minor axis is the highest, and the radial velocity component in these directions is zero. Finally, their fourth hypothesis is to use a infinitely thin disk, such that they can guarantee the same inclination for observed velocities at a projected r in equation (2.6.4) . Using these assumptions they applied a minimization method to fit the model to

the observational data (velocity field) of the NGC 2976 galaxy, favoring a non axisymmetric flux with an inclination of 17° with respect the mayor axis, which gave them evidence about the existence of a bar in this galaxy. This method can be applied to model any spiral galaxy velocity field because the velocity fit depends merely on geometrical parameters which could be well determined by the photometry or even with the minimization routine implemented in the bi-symmetric model fit (See section 7 for more detailed information)

We decided to apply this modeling method to our observed velocity fields. As a reference we initially studied all the velocity field assuming a rotation only model. Later, for the HI we investigated the nature of lopsidedness, after we concluded that the asymmetry is not created by a warp using the tilted ring technique, this experiment will set the disk global geometry. For $H\alpha$ and CO we tried all the available kinematic decompositions, because as it is shown in the upper right panel of Fig. 6) and the upper right panel of Fig. 10 their emission shows a complex structure.

2.7. Results

2.7.1. Choosing a Best Model Velocity Field

We present the results of the modeling technique applied to the $H\alpha$, CO and HI velocity fields given by the Fourier decomposition in figures (Fig. 6 to 9) for $H\alpha$ emission, (Fig. 10 to 11) for CO emission, and Fig. 12 to 13 for HI emission.

In the case of the observed $H\alpha$ velocity field (upper right panel of Fig. 6) the presence of a bar distortion in the central region is very noticeable. The effect of a non-axisymmetric potential in the velocity field is very well reproduced by the global m=1 model as it is shown in the figure (bottom left panel of Fig. 7) In the bar-affected region the field is not rotating as it would be expected in a pure rotation model, instead we can see a very

complex kinematic behavior (the model corresponding to rotation only is presented in appendix G). This is a first confirmation that the assumptions of pure rotation models does not describe the nature of the kinematics in barred galaxies potentials.

Analyzing the CO model velocity fields (bottom left panel of Figs. 10, 11) we can observe that the bi-symmetric model reproduces the global rotation in the outer region. However, as it is shown in the upper right panel of the Fig. 10 the central region the CO observed velocity field shows very low velocity gradients that can not reproduced by the m=2 model, meaning that any interpretation should be done carefully.

In the bottom right panel of Figs . 10 and 11) we show the substraction between the modeled and observed velocity fields for the CO emission. We can see that the residual velocity values are a small fraction of the corresponding velocity fields, meaning that both the lopsided and the bi-symmetric model make reasonable fits to the data.

In the case of HI data we decided to apply the $m = 1$ and $m = 2$ models shown in Figs. 12 and 12). We noticed that for this extended region the best fitting model corresponds to the $m = 1$ mode, indicating that the most important perturbation is due to a lopsided mode. For the HI tracer it was easier to choose an appropriate model because the residual map for the lopsidedness perturbation (bottom right panel of Fig. 12)are considerably smaller than the one for the bi-symmetric model (bottom right panel of Fig. 13).

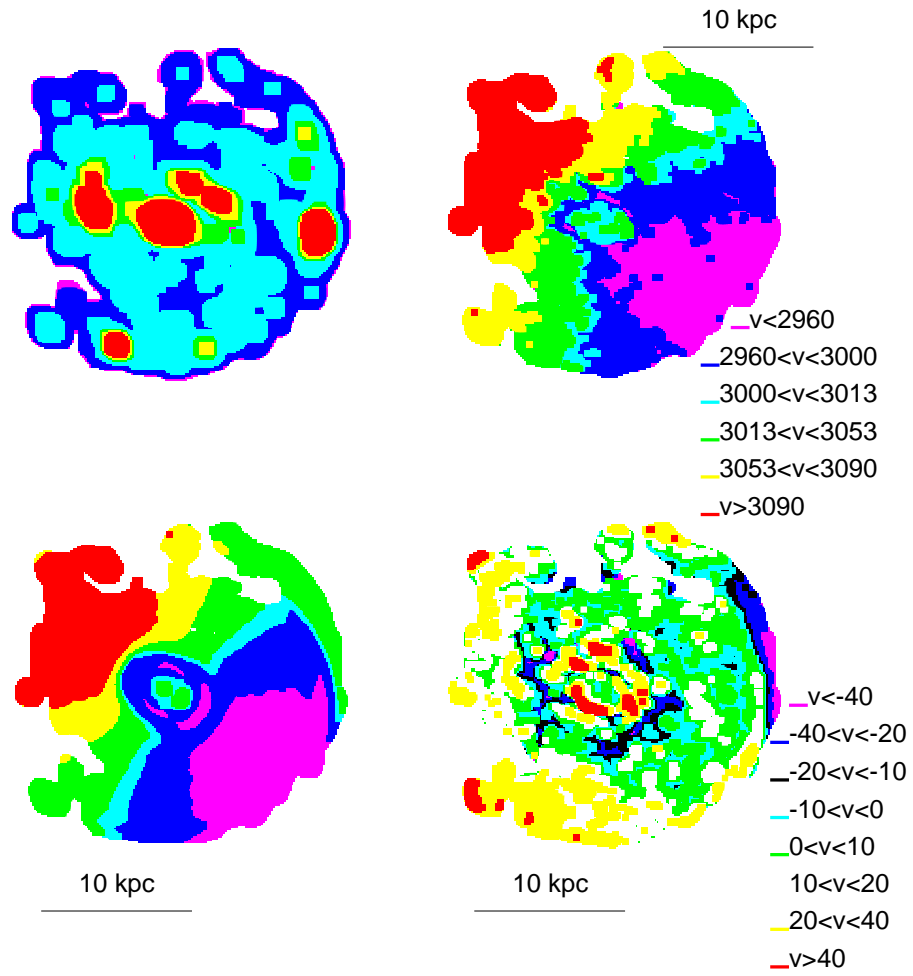The parameters obtained in the minimization for the chosen models are shown in the table 2.7.1.

10 kpc

v<2960

2960<v<3000

3000<v<3013

3013<v<3053

3053<v<3090

v>3090

10 kpc

10 kpc

v<-40

-40<v<-20

-20<v<-10

-10<v<0

0<v<10

10<v<20

20<v<40

v>40

Fig. 6.— $H\alpha$ lopsided m=1 modeling results. Up: image (left), velocity field (right). Bottom: modeled velocity field (left), Residual map (right). Velocities are given in km/s
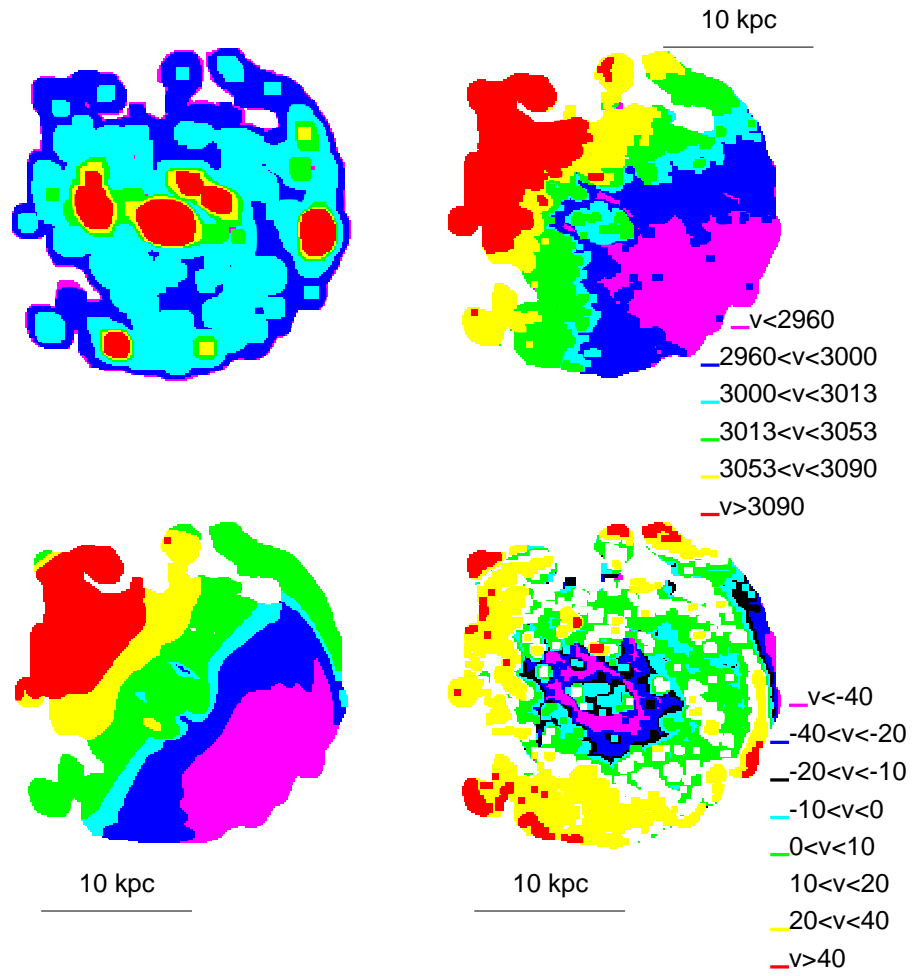
Fig. 7.— $H\alpha$ by-symmetric m=2 modeling results. Up: image (left), velocity field (right). Bottom: modeled velocity field (left), Residual map (right). Velocities are given in km/s
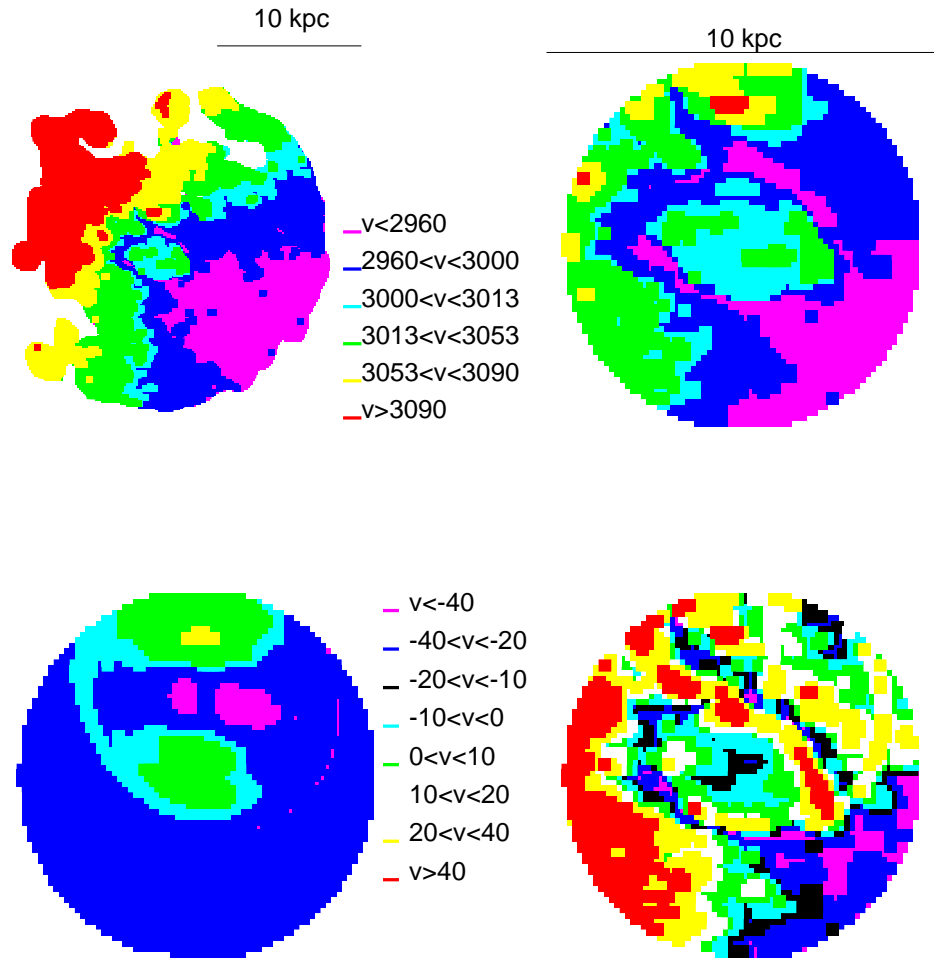
Fig. 8.— $H\alpha$ central region lopsided m=1 modeling results. Up: velocity field (left), central region of the velocity field (right). Bottom: modeled velocity field (left), Residual map (right). Velocities are given in km/s

10 kpc

10 kpc

v<2960
2960<v<3000
3000<v<3013
3013<v<3053
3053<v<3090
v>3090

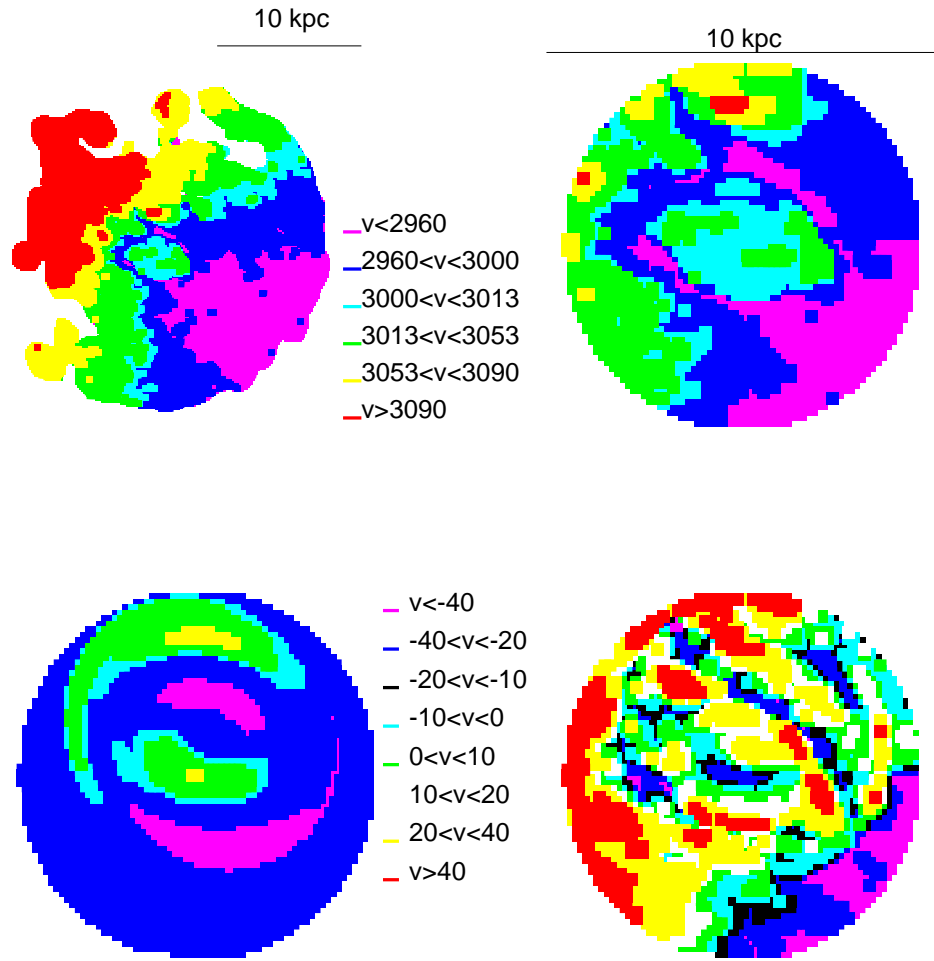v<-40
-40<v<-20
-20<v<-10
-10<v<0
0<v<10
10<v<20
20<v<40
v>40

Fig. 9.— $H\alpha$ central region by-symmetric m=2 modeling results. Up: velocity field (left), central region of the velocity field (right). Bottom: modeled velocity field (left), Residual map (right). Velocities are given in km/s
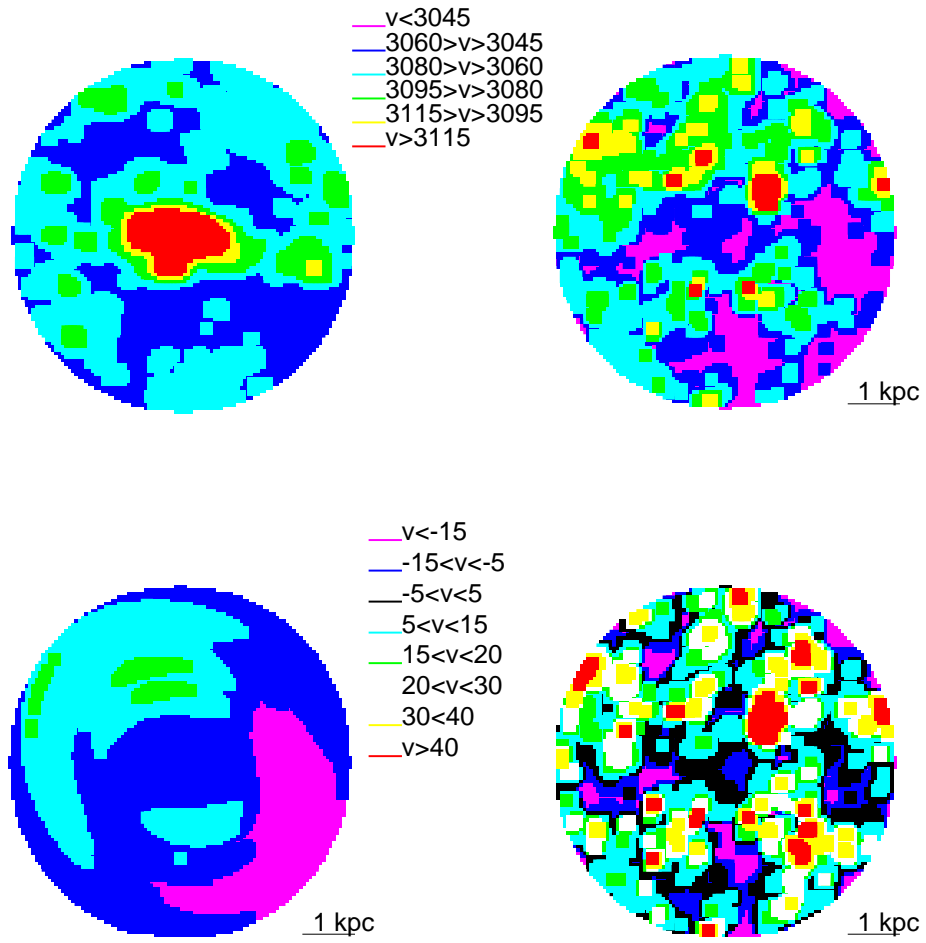
Fig. 10.— *CO* lopsided m=1 modeling results. Up: image (left), velocity field (right). Bottom: modeled velocity field (left), Residual map (right). Velocities are given in km/s

Fig. 11.— *CO* by-symmetric m=2 modeling results. Up: image (left), velocity field (right). Bottom: modeled velocity field (left), Residual map (right). Velocites are given in km/s
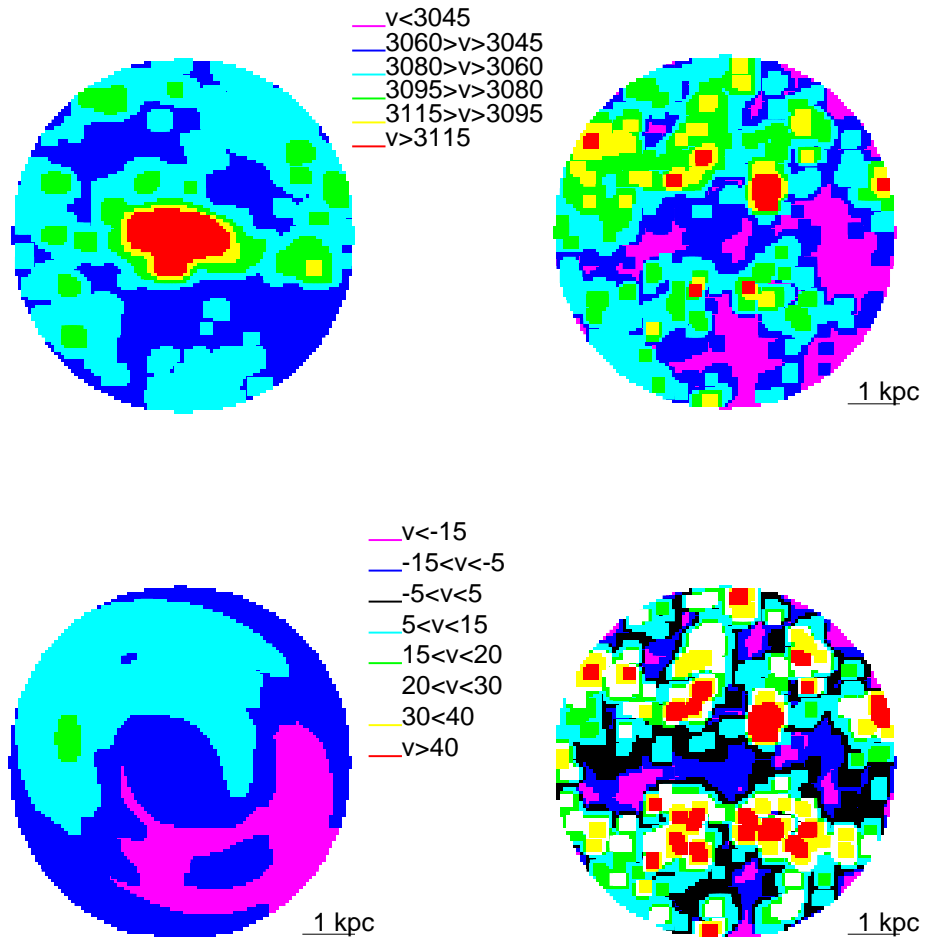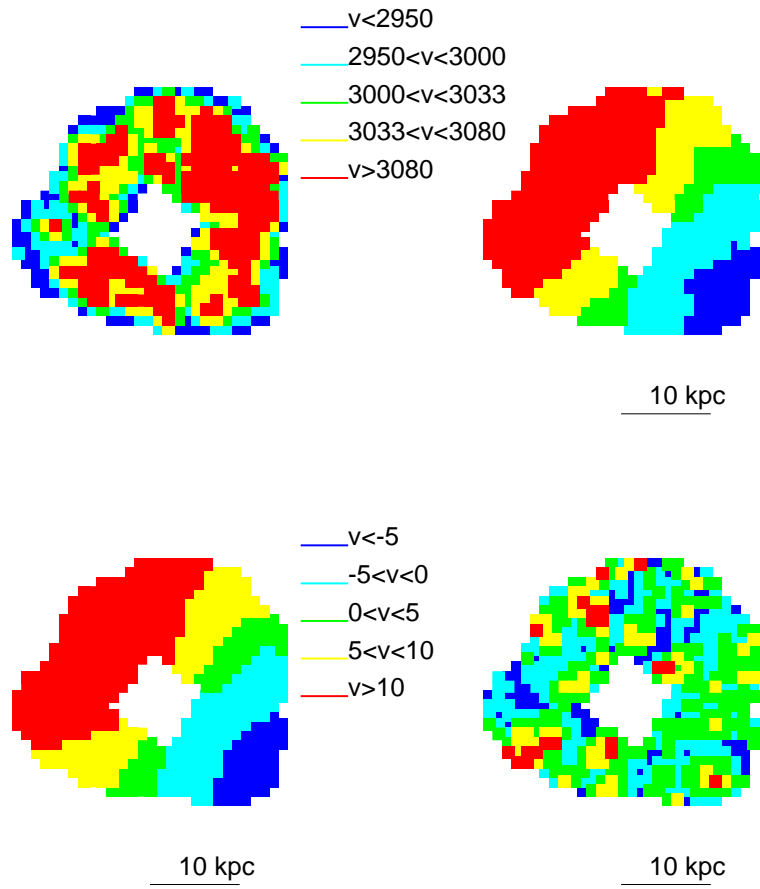
Fig. 12.— *HI* lopsided m=1 modeling results. Up: image (left), velocity field (right). Bottom: modeled velocity field (left), Residual map (right). Velocities are given in *km/s*
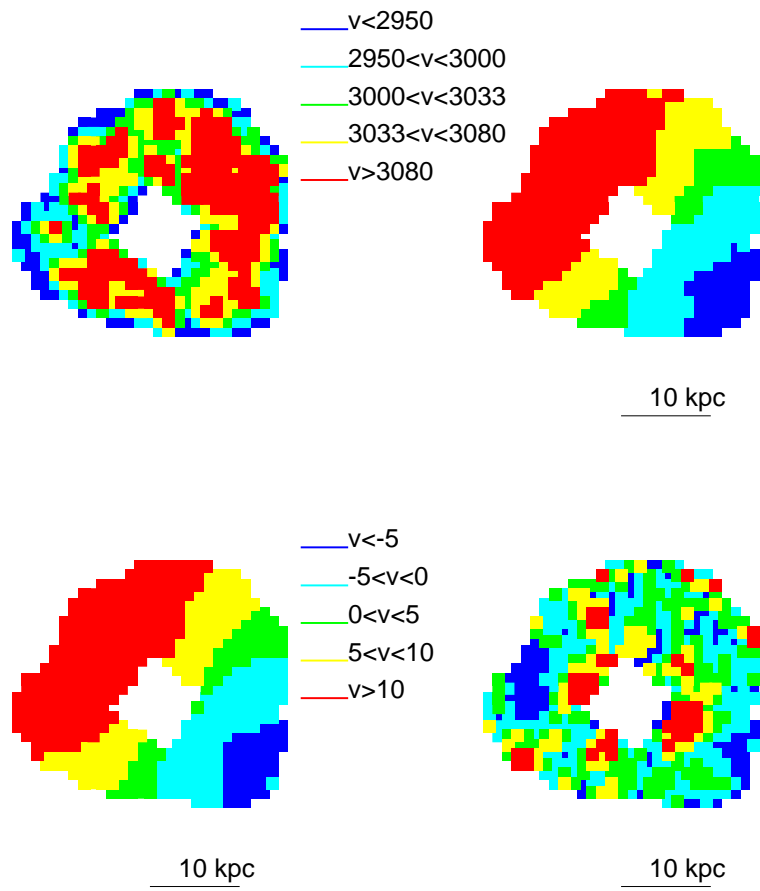
Fig. 13.— *HI* by-symmetric m=2 modeling results. Up: image (left), velocity field (right). Bottom: modeled velocity field (left), Residual map (right). Velocities are given in *km/s*

Tracer	Model	Center	minimum χ^2	Adjusted bar $P.A$	Adjusted V_{sys}
HI	m=1	free	0.22	—	3069.10
HI	m=2	fixed	0.38	13.77	3040.91
HI	rotation only	free	0.42	—	3041.28
$H\alpha$	m=1	free	0.25	—	3029.51
$H\alpha$	m=2	fixed	0.43	62.52	3020.58
$H\alpha$ central region	m=1	free	0.58	—	2974.37
$H\alpha$ central region	m=2	free	0.55	6.79	2983.12
$H\alpha$ central region	rotation only	free	0.74	—	2983.36
CO	m=1	free	2.04	—	3057.80
CO	m=2	fixed	2.02	55.07	3054.12

2.7.2. Rotation curves

Besides the modeled velocity maps, it was possible to built the rotation curves for all of the models. This analysis make possible to compare with previous kinematic studies of NGC 3367.

In Fig. 14 we show the rotation curve of an only rotation modelling with a set of input parameters, such as $i = 28$, $P.A = 51.6$ and $Vsys = 3027.0 km/s$. For the Figures (Figs. 15, 16) we also show the rotation curves for the same input parameter set.

In Fig. 17 we show the $H\alpha$ rotation curves for the $m = 1$ and $m = 2$ Fourier modes adjustment, as well as the model non circular motions in their radial and tangential components. It is clearly shown that for the bi-symmetric mode the amplitude of those non circular motions are similar to the velocities of the inner region of the rotation curve. However for the lopsided mode the amplitude of the non circular motions are evidently

greater than the velocities of the inner region of the rotation curve.

We also show a plot for the noncircular motions for the three tracers (Fig. 21).
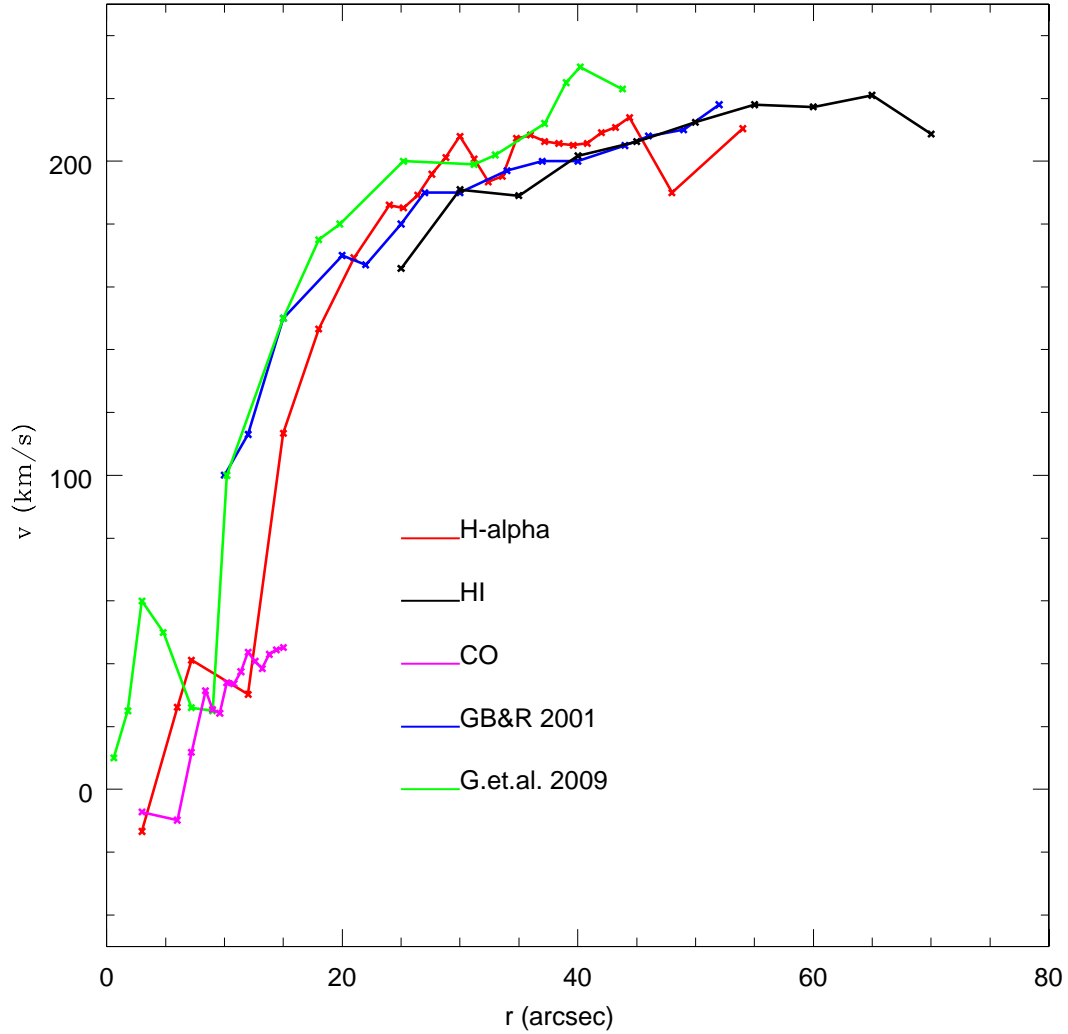

Fig. 14.— Rotation curves for the three used kinematic tracers when an only rotation modelling is used. We also compare our results with previous works rotation curves.
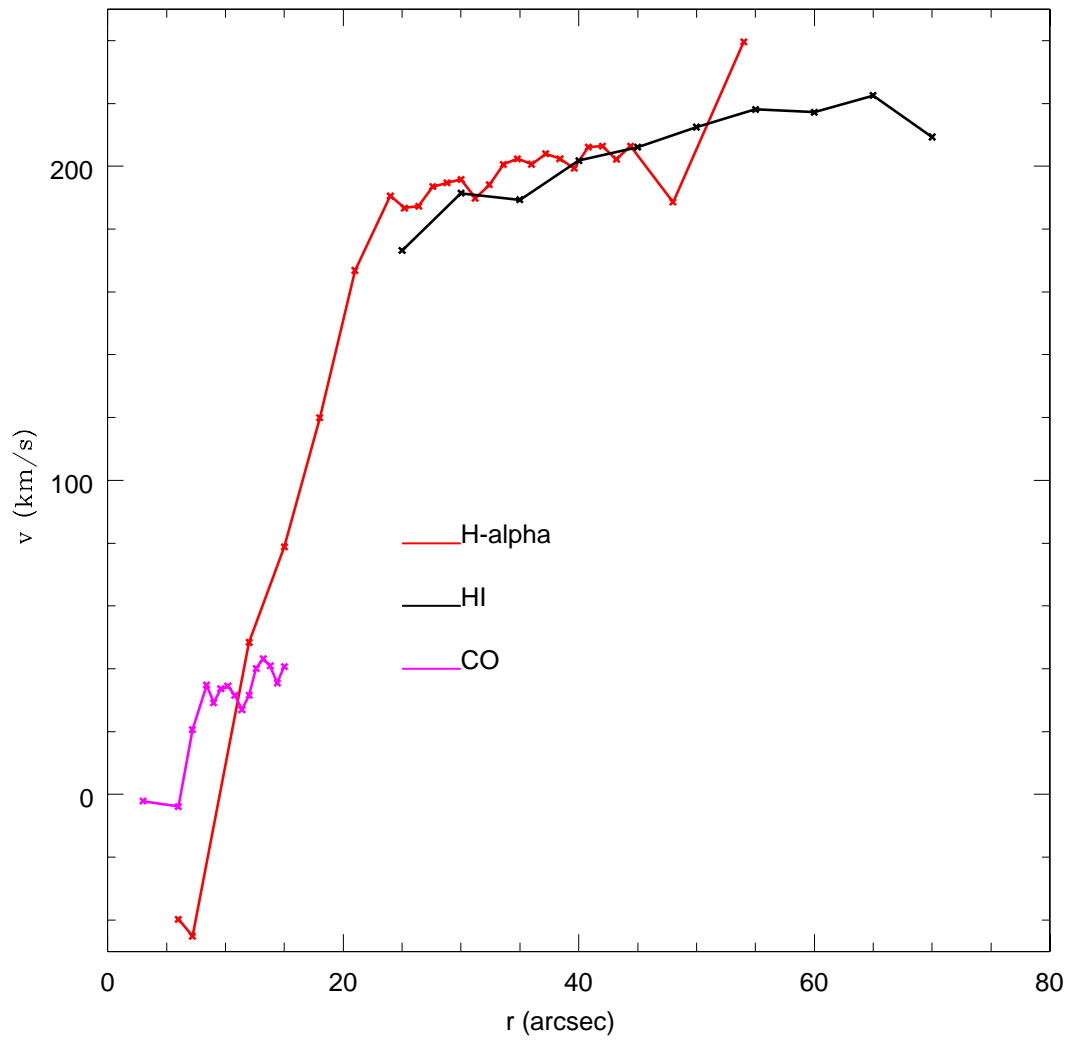
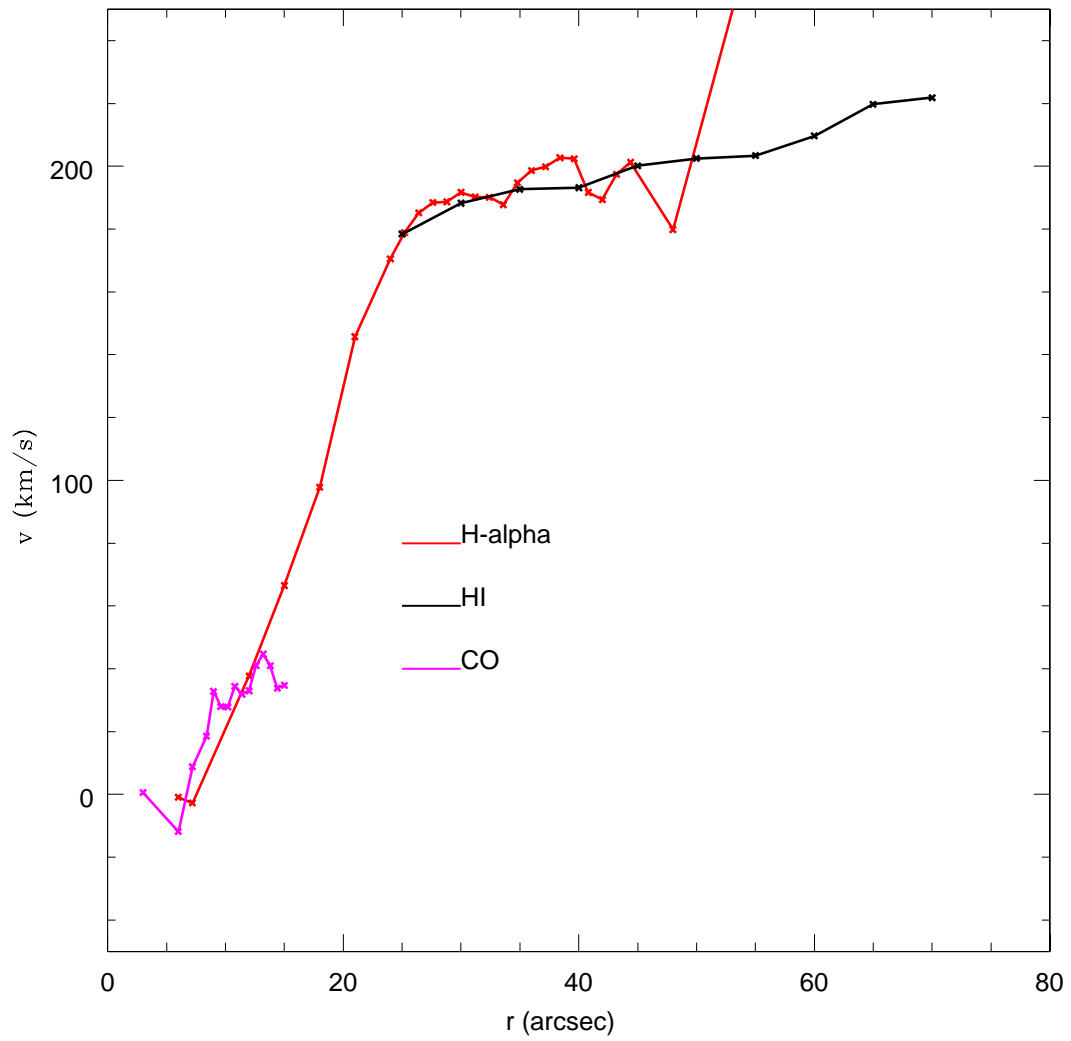Fig. 15.— Rotation curves for the three used kinematic tracers when a lopsided modelling is used.

Fig. 16.— Rotation curves for the three used kinematic tracers when a bi-symmetric modelling is used.

Fig. 17.— Up: $m = 2$ $H\alpha$ rotation curve and its non circular motions. Bottom: $m = 1$ $H\alpha$ rotation curve and its non circular motions.

Fig. 18.— Upper panel: Non circular motions for HI $m = 1$ mode. Middle panel: Non circular motions for $H\alpha$ $m = 2$ mode. Bottom panel: Non circular motions for CO $m = 2$

2.7.3. Velocity jumps across the bar

The Inter Stellar Medium shocks caused by the bar are a distinctive kinematic feature, in contrast to non-circular motions that may have multiple origins besides the bi-symmetric

perturbation. The shocks can be characterized by the amplitude of velocity jump across the bar, but also by the shock geometry traced by the dust lanes. In the photometry section we used a B-I color map in order to increase the dust lanes c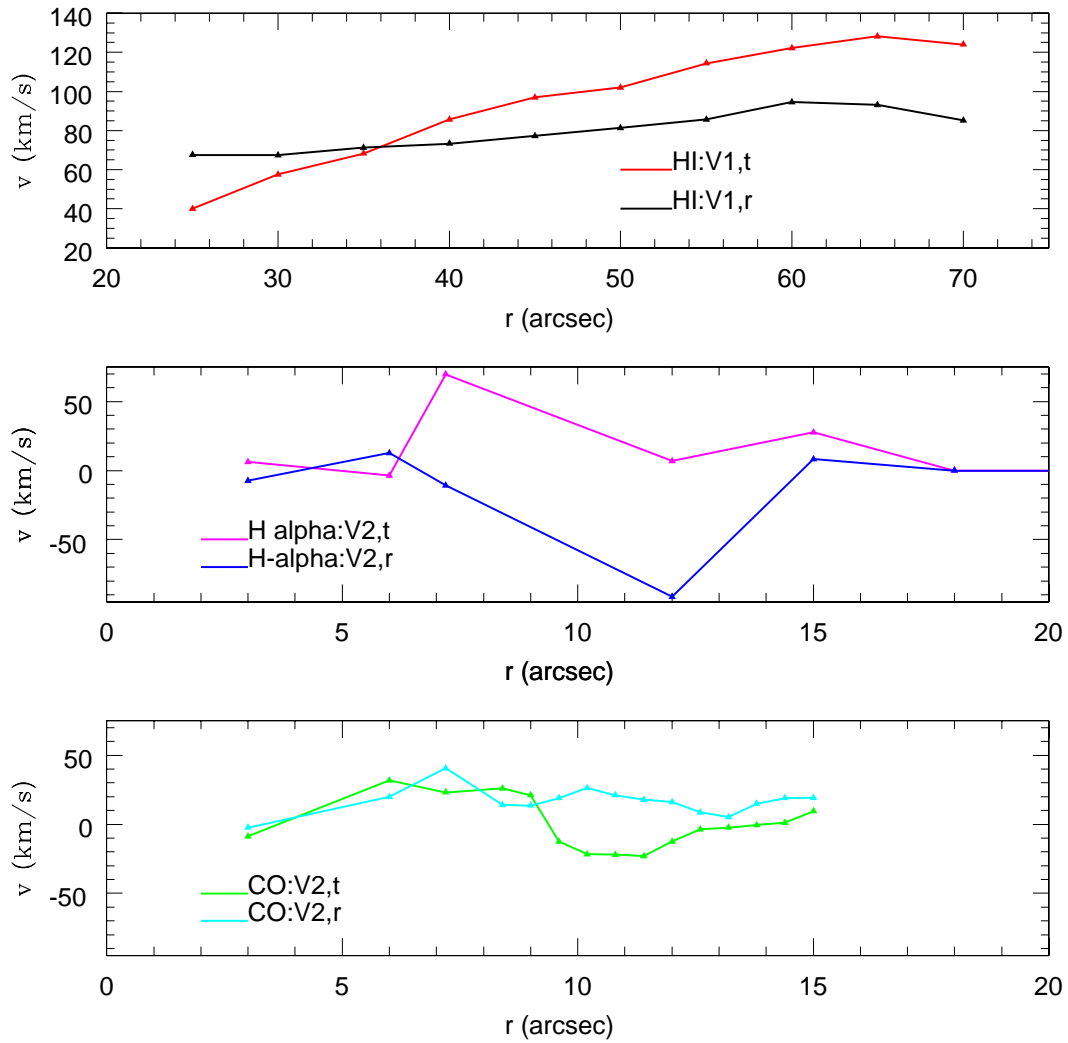ontrast over the galaxy disk. We notice that the the dust lanes are not parallel to the bar position angle. However the interpretation is ambiguous because the ISM reaction depends on the bar mass, strength, speed and the ISM effective equation of state. Although in paper I the bar strength was constrained, the bar mass depends on the stellar M/L ratio, and thus extra quantities are needed in order to brake the degeneracy. In order to solve the problem we measured the velocity jumps, see figures 19 and 20 in which we we can observe a line of sight velocity gradient when we cross the bar region from the South to the North side of the velocity field. The pattern speed has been recently reported by Gabassov et al 2009. The last missing step is not trivial, because the dependence of the ISM kinematic reaction to the bar is not lineal, therefore it will require simulations in order to give a final answer. We postpone to a future paper this analysis.

Fig. 19.— Velocity jump across the bar at the left side of the galaxy center.

shock at 12.6 arcsec from galaxy center
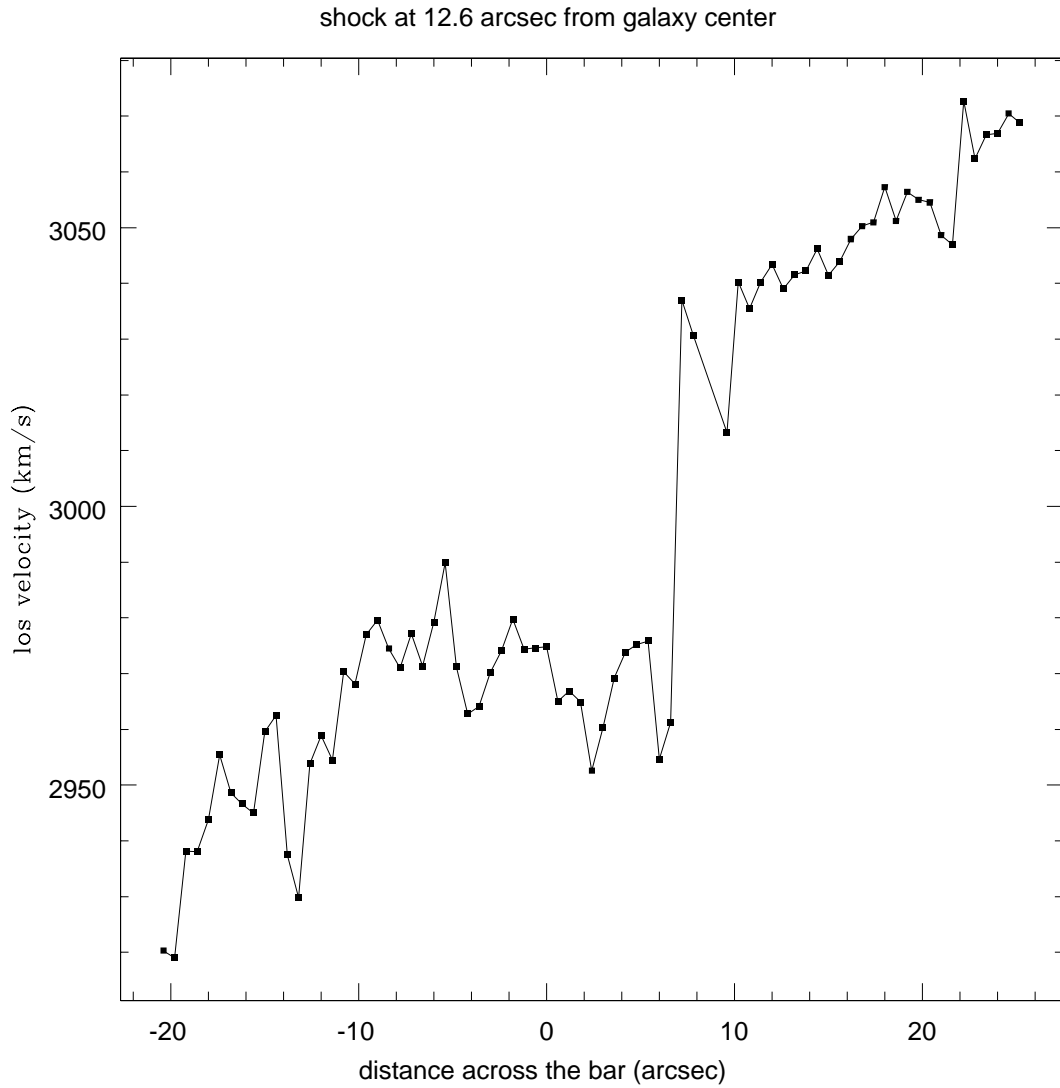

Fig. 20.— Velocity jump across the bar at the right side of the galaxy center.

2.8. Circular Velocity Decomposition

After obtaining rotation curves based on different models for the non-circular motions. We are interested to evaluate the goodness of each curve as an estimator to the galaxy circular velocity. We are also interested about the possible constraints to the dark matter

distribution and possible comparisons to the predictions of adiabatic contraction.

Figure 21 compares the $H\alpha$ and HI rotation curves against a circular velocity curve derived from the observed 3.6 μm surface brightness density. For the sake of an initial discussion, the plot is divided basically into three regions according to the disk scale length in 3.6 μm. In the inner region (radii lower than $20 arcsec$) a deficit of the $H\alpha$ rotation curve is observed when compared to that of the circular velocity curve. This is not surprising since a major contribution coming from non-circular motions is inferred precisely there (see Section 2.7). The 3.6 μm circular velocity map (Figure 5) shows that in the inner region, the major contributors to the observed circular velocity come from the bar and inner arms region, consistent with the idea that such structures are behind strong-non-circular motions. On the other hand, the opposite is observed in the outer region (radii beyond $20 arcsec$) where the circular velocity curve shows a strong deficit when compared to the $H\alpha$ curve, suggesting that the circular velocity traced by the stellar component of the galaxy does not fully describe the kinematics of the whole galaxy potential (baryonic and dark matter contribution) traced by the $H\alpha$ rotation curve. The third region is the transition zone at one scale-length ($\sim 20 arcsec$) which shows comparable contributions coming from both the circular velocity and $H\alpha$ curves. Naively we can conclude that at one radial scale length the baryonic and dark matter content are comparable, which is consistent with models of disk galaxy formation (adiabatic contraction). However, the main conclusion is that such a simplistic rotation curve analysis is not accurate enough to evaluate these predictions. A full dynamical model subject to the rich kinematics measured in this paper is required.
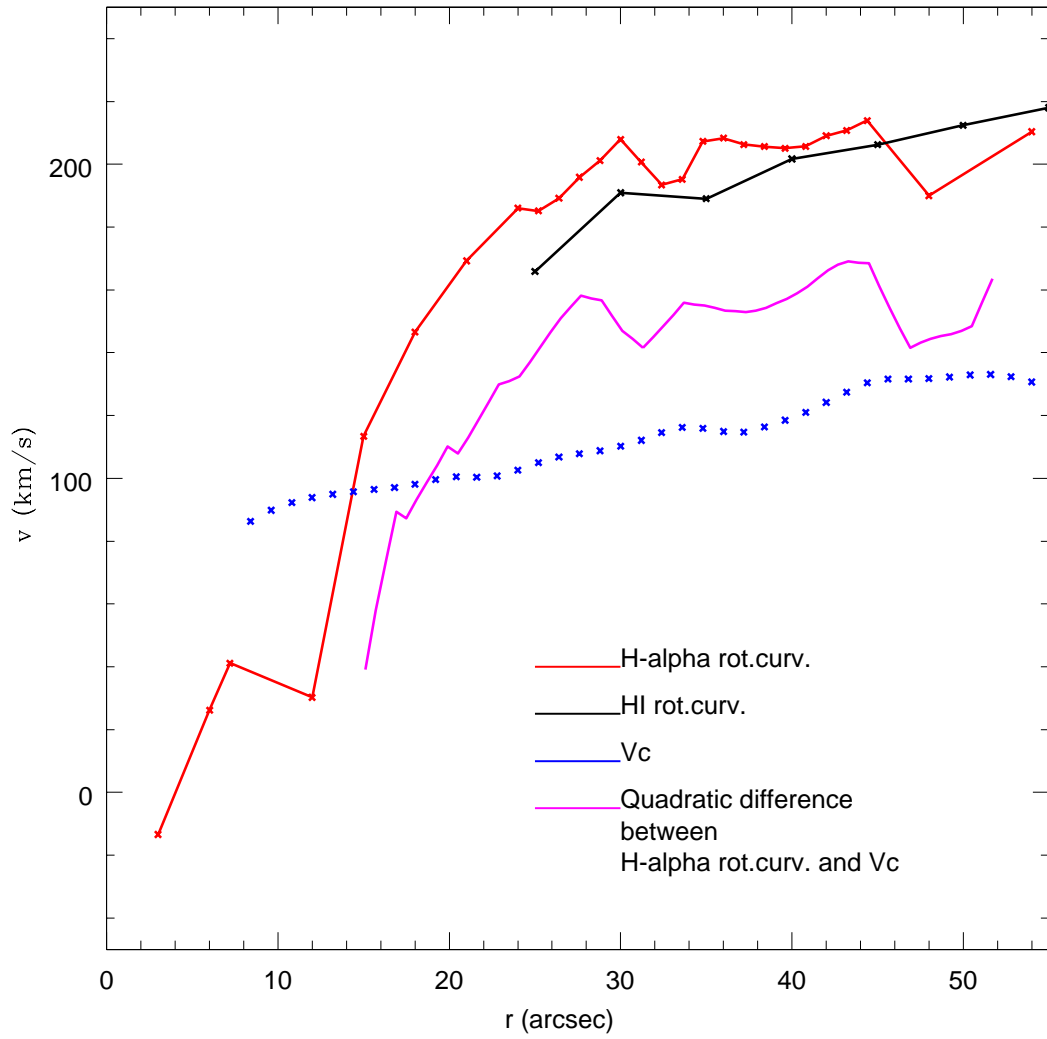
Fig. 21.— In this plot we compare the $H\alpha$ and HI rotation curves (red and black) with a circular velocity curve (blue). We also show the quadratic difference between the $H\alpha$ rotation curve and the circular velocity one.

2.9. Discussion

The model with the smallest residual field assumes a lopsided geometry at scales larger than 20 arcseconds. Inside this region ionized gas suggest a bi-symmetric geometry but CO marginally favors a lopsided kinematics over a bi-symmetric one. (**?**) previously reported the evidence of a CO cloud in the central region, this could explain the counter rotating feature in the CO central model which is absent in H-α data model. If we assume this explanation is true, NGC 3367 kinematics is centrally dominated by the bar perturbation and in the external region by a lopsided kinematics. The large m=1 radial and tangential velocity components suggest that the asymmetry is created by extraplanar gas, this explanation also follows (García-Barreto & Rosado 2001) and (Hernández-Toledo et al. 2009) discussion. Currently we are unable to decide between a tidal tail or gas accretion, however the absent of a massive companion favors the accretion model.

A corollary of the favored kinematic model is that NGC 3367 is a suitable case for dynamical analysis.

For all considered models the poorest fit corresponds to the one that includes only rotation velocities, this confirms that previous constraints using only rotation curves are rather weak. Dissecting the central kinematics just as we do in this study will allow us to do a robust estimation of the disk mass and to have a better estimation of the dark matter concentration with respect to baryonic matter.

In Hernández-Toledo et al 2009, we reported extraplanar gas detected by the velocity channels in H-α and HI velocity fields. The gas rich morphology and the current star formation activity supports the possibility of gas accretion. The isolated environment is consistent with gas accretion by large scale filaments as discussed by (Dekel & Birnboim (2006), Dekel et al. (2009), Bournaud & Elmegreen (2009), Dekel et al. (2009), Sales et al. (2009) and Agertz et al. (2009). If this is confirmed, NGC 3367 provides possible evidence

of connection between large scale gas accretion and nuclear activity.

A few words about uncertainties must be said. There are two kinds error sources in our estimation of NGC 3367 properties. First, random errors related to the accuracy of measurements. We can classify this kind of errors based on the photometric or kinematic tracer:

HI (VLA): 11 km/s instrumental.

Hα: (Fabry-Perot) 10 km/s (channel width).

CO: 10 km/s (channel width).

Photometry: An analysis of the errors in a 2D large-aperture photometric measurement shows 2 major contributors. First the ones associated to the zero-point scale and color terms of a photometric transformation and second the ones coming from a major contribution of the sky at large apertures. On earth-based observations at 2.1 μm that ranslates into 0.15-0.25 mag. For Spitzer observations, conservative errors are 0.1 - 0.15 mag.

There is however another class of uncertainties, systematic errors. In our case they are mostly related with the limitations of measurements techniques or models used to make interpretation of observations. Example of this kind of uncertainties are the role of non-circular motions, the existence of non-gravitational forces (like pressure gradients). The stellar mass to light ratio for a galaxy disk. In the current study we focused our analysis on the full kinematic dissection of the galaxy disk. We found that non-circular motions are comparable to the amplitude of rotation at around one radial exponential scalelenght. Accurate estimations for the stellar M/L ratio with accuracy better than a factor of 1.5-2 are difficult. Because of that we consider that showing the formal instrumental error bars are not truly informative. Instead, we would like to point out that the kinematic and photometric quantities that we have estimated are able to constraint the stellar M/L ratio

independently of stellar population models using dynamics. Once we do this kind of analysis we will be able to set robust constraints on the central matter content in NGC 3367.

2.10. Conclusions

The best fit models in the inner galaxy region indicate that NGC 3367 is well described by a bi-symmetric kinematics and therefore is a good case for a dynamical analysis. The large scale asymmetry might be created by extraplanar gas, likely the result of cosmic accretion. If confirmed, this scenario suggest that AGN activity might be correlated with gas filament accretion.

3. Conclusiones

De todos los modelos considerados el peor ajuste tanto por el valor de la χ^2 reducida como por la geometría del campo de velocidades, corresponde al que incluye sólo rotación, esto confirma que restricciones previas usando sólo curvas de rotación son débiles. Disectando la cinemática central como lo realizamos en este estudio abre la posibilidad de dar una estimación robusta de la masa del disco así como tener una mejor estimación de la concentración central de materia obscura con respecto a la materia bariónica.

La cinemática de las regiones interna de la galaxia NGC 3367, son razonablemente bien descritos por un modelo bisimétrico, eso confirma que esta galaxia es un buen caso para estudios dinámicos. Las asimetrías a gran escala en el campo de velocidades ($m = 1$) se deben probablemente a gas fuera del plano, esto debido a la gran amplitud de las velocidades radiales y tangenciales del centro cinemático con respecto al centro geométrico que se requeririan (Fig. 21). La cinemática central de los diferentes trazadores está dominada por movimientos no circulares, lo cual debilita estudios en los que sólo se ha utiizado la curva de rotación. La caracterización cinem ática de nuestro estudio servirá para construir un modelo de la estructura central de NGC 3367. El origen de este material fuera de plano puede ser un puente de marea, sin embargo, estudios fotométricos en los alededores de la galaxia (SDSS,Hernández-Toledo et al. (2009)) excluyen la presencia de un compañero masivo respecto al disco. Alternativamente el gas se puede deber a acreción cósmica, esto ya se ha argumentado anteriormente en conexión al origen de anillos polares y asimetrías en galaxias ($m = 1$). Si estudios futuros de campo amplio y alta sensibiliad en HI verifican este escenario, el caso de NGC 3367 sugeriría una posible conexión entre la accreción cósmica de gas y la actividad central de algunas galaxias.

Complementar este análisis es necesario, para ello tenemos como trabajo a futuro analizar observaciones de espectroscopía estelar en la barra de NGC 3367, las cuales ya han

sido adquiridas en el 2008 con la colaboración del Dr. Jesús González González. A partir de ello podremos hacer una estimación de la rotación y de la dispersión de velocidades, lo cual decidirá si la presencia de fuerzas no gravitacionales es importante. Dichas observaciones nos permitirán estimar la frecuencia de rotación de la barra por el método Tremaine-Weinberg (Tremaine & Weinberg (1984)). También es necesario comparar nuestros resultados con las predicciones para modelos de interacción dinámica entre bariones y materia obscura. También será necesario realizar estudios similares para muestras de galaxias en diferentes ambientes y corrimientos al rojo.

4.   Appendix A: Adiabatic Contraction

This models describes the dark matter halo response to the baryonic collapse, like the disk formation process (see Blumenthal et al. (1986); Gnedin et al. (2004)).

The basic concept behind this model is the existence of conserved quantities if the collapse characteristic time is larger than the typical dark matter particle orbital time, this is the meaning of adiabatic in this model.

This model assumes that the disk could be described as a sphere with the same mass profile, that the baryonic collapse within the halo is adiabatic, that the angular momentum is conserved, and that the dark matter halo particles follows circular orbits(Blumenthal et al. (1986)). These assumptions lead to relate the initial and final states of the halos as follows:

$$r_i M_{i,total}(r_i) = r_f(M_{f,disk}(r_f) + M_{f,halo}(r_f)), \qquad (4.0.1)$$

where $M(r)$ is the mass inside a radius r, and the subscripts i and f indicates the initial and final states of the shown quantities.

The mayor implication of this model is that the dark matter halos are contracted during formation by the baryons infall resulting in inner density profiles with smaller core radii and higher central densities.

There are models that do not require circular orbits, for example Gnedin et al. (2004) model enable elliptical orbits.

Colín et al. (2006) show that the bar formation process also triggers a dark matter constraction. This process is well described by the Gnedin et al. (2004) model.

Recent studies in a cosmological context suggest that the amount of contraction

depends on the individual galaxy dynamical history.

5.   Appendix B: Photometry

As we have stated in the text we worked with photometric $UBVRIJHK$ bands as well as 3.6, 4.5 and 5.8 μ observations.

The image processing involved subtraction of the bias, division by flat-field frames, subtraction of sky frames, and registration of the images to a common coordinate system. A master flat-field frame for each filter was built by stacking several night-sky subtracted twilight frames in the corresponding filters. The resulting combined images were aligned to within 0.2 pixels through a geometrical mapping using the GEOTRAN and GEOMAP tasks available in the IRAF reduction software. The routines under Space Telescope Science Data Analysis System (STSDAS) were used in the reduction and analysis of both the optical and near-IR data.

We obtained surface brightness (SB) profiles by elliptical isophote fitting with fixed center using also routines under the STSDAS package. This procedure is based in an interactive method described by Jedrzejewski (1987) where initial values of the parameters (center, ellipticity and position angle) are required as a first guess in order to produce an intensity distribution along the isophotes as well as a fitting of the same parameters in each elliptical isophote.

6.   Appendix C: Photometry Published Results

The reduction of the photometric images, as have been stated in section 2.4 was a fundamental basis for the kinematic study of NGC 3367, however, the results reported in

that section were just a part of a larger analysis, that have been already reported in paper (Hernández-Toledo, et.al. 2009 in revision). As some of those results are not directly linked to the kinematical analysis developed here, we decided not to include them in the section 2.4. However as the photometric analysis was the first approach of this study we include in this appendix the abstract of our Photometry paper as well as link to read it if it is of the reader interest.

A Structural Analysis of the Isolated Active Galaxy NGC 3367:Disk, Bar and Lopsidedness

Abstract:

NGC 3367 is a nearby active galaxy that shows a strong bar and evidence of lopsidedness despite its isolation. In this paper we present a quantitative analysis of its disk structure. Our study is based on new Optical $UBVRI$ and NIR JHK images obtained with the 0.84m and 2.1m telescopes at OAN-SPM. From 1D and 2D bulge/disk decomposition analysis, an exponential bulge is obtained in all the observed bands. The disk scale length in the U and B bands is 2.9-2.0 times larger than that in the K band, consistent with a central B-band optical depth as high as 15. Color profiles show that the external disk is bluer. The bar strength (Q) parameter value is in the highest range (4-5) in Buta & Block (2001) classification as obtained from the ratio of tangential and radial forces. The $B - I$ color map reveals a prominent curved dust lane. Its geometry suggests that the bar might not be as fast as in early type galaxies, however a final assessment needs also to consider the internal galaxy kinematics. The lopsidedness in NGC 3367 is studied through various indicators, namely i) the CAS indexes and structural diagrams frequently used in high redshift galaxies, estimated in the optical and NIR light, ii) the Fourier modes amplitudes of the stellar surface density also estimated in NIR/Optical bands, commonly used for nearby resolved galaxies and finally iii) the HI gas distribution of the disk from the

integrated VLA HI profile. The value of the Lopsidedness/Asymmetry found using the red stellar component is ~ 0.1, which is close to the average value found in the Local Universe, however the HI and blue stellar component show a larger asymmetry. We discuss different scenarios for the origin of the bar/lopsidedness and possible connections with the galaxy recent accretion history.

Link to the paper: http://www.astroscu.unam.mx/$\sim$octavio/

7. Appendix D: Tilted rings implementation and Velfit code

The method of the tilted rings model described in section 2.6.1 is a very well and used model in extragalactic astronomy. Its usage is directly applicable to a galaxy velocity field. One example of the application of this method is available to use in the Analyse et Depouillement Homogene des Observations Cigale (ADHOC) software (http://www.oamp.fr/adhoc/adhocw.htm). The most common distribution of this free software is for Windows XP operative systems. Where the fitting in rings regions is done automatically using some input parameters such as position angle, inclination, center, systemic velocity and rings radius performing the method described in section 2.6.1 over the galaxy velocity field (see figure. 22). This software fits the mentioned parameters in order to obtain a minimum χ^2

The velfit software is a code that implements the method explained in the paper by Spekkens & Sellwood (2007). The main idea behind this code is that the velocity of any particle in a galaxy has a tangential and a rotational components, and each of them could be described as a Fourier series around a circle of radius r. Considering also the galaxy inclination and its systemic velocity V_{sys}, the line of sight velocity of each particle it is described by equation (7.0.2)
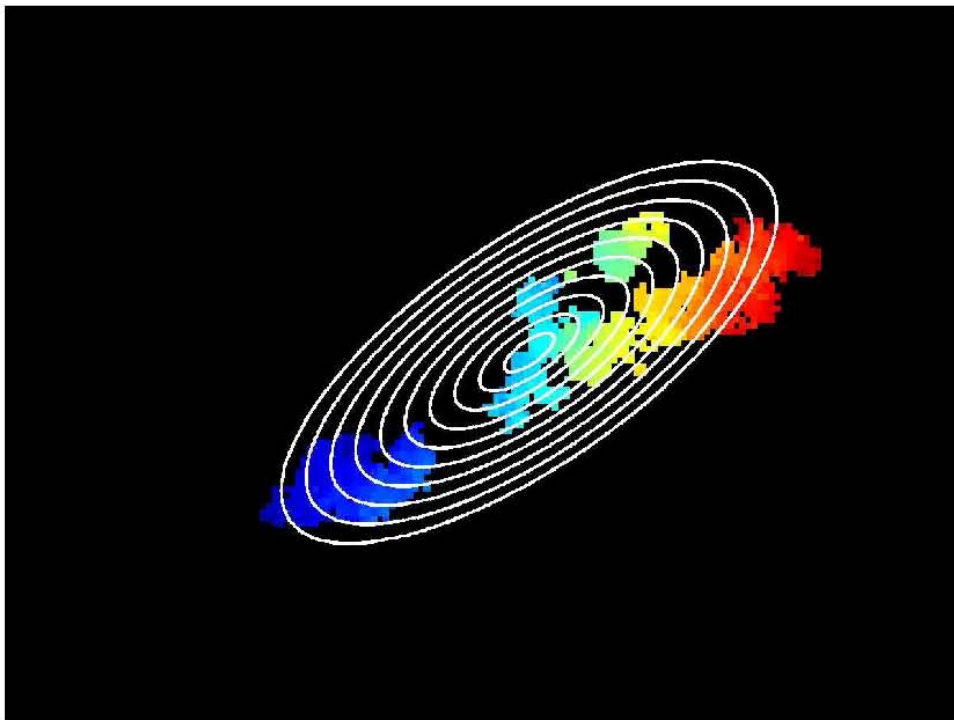
Fig. 22.— Representation of the Tilted Rings model over a galaxy velocity field.

$$V_{obs} = V_{sys} + \sin(i) \left[\begin{array}{l} \overline{V_t} \cos\theta + \sum\limits_{m=1}^{\infty} V_{m,t} \cos\theta \cos(m\theta + \theta_{m,t}) \\ +\overline{V_r} \sin(\theta) + \sum\limits_{m=1}^{\infty} V_{m,r} \sin(\theta) \cos(m\theta + \theta_{m,r}) \end{array} \right], \tag{7.0.2}$$

where m is the Fourier mode and θ is the position over the circle. From this equation we can derive three different models besides the only rotation model.

The first one is the lopsided model $m = 1$, given by equation (7.0.3)

$$V_{model} = V_{sys} + \sin(i) \left[\overline{V_t} \cos\theta - V_{1,t} \cos(\theta_b) \cos(\theta) - V_{1,r} \sin(\theta_b) \sin(\theta) \right] \tag{7.0.3}$$

The second is the bi-symmetric model $m = 2$, given by equation (7.0.4)

$$V_{model} = V_{sys} + \sin(i) \left[\overline{V_t} \cos\theta - V_{2,t} \cos(2\theta_b) \cos(\theta) - V_{2,r} \sin(2\theta_b) \sin(\theta) \right] \tag{7.0.4}$$

And the third one is called the radial model $m = 0$, given by equation (7.0.5)

$$V_{model} = V_{sys} + \sin(i) \left[\overline{V_t} \cos\theta + \overline{V_r} \sin\theta \right] \tag{7.0.5}$$

Velfit code is able to fit any of those models to a velocity field using a fitting technique described in Barnes & Sellwood (2003) that determines a set of parameters such as the systemic velocity $Vsys$, the position angle $P.A$, the inclination i, ellipticity ϵ, the center of the galaxy (x_0, y_0), the fixed disk $P.A$ of the non-axisymmetric perturbation (θ_m) and M unknown radial functions $V_{m,r}$ and $V_{m,t}$. The model parameters are adjusted to get a minimum χ^2 of the standard goodness of fit function χ^2 with ν degrees of freedom. Then all of the M independent velocity profiles are tabulated in a set of concentric rings that will

be projected to ellipses on the sky. Once that is done we are able to generate a velocity model to each point of the velocity field.

8. Appendix E: FITS Images

The FITS files format (Flexible Image Transport System) allows to store and manipulate astronomical (or other kind) of images (see Wells et al. (1981)). Every person can read, create and modify any FITS type image by using standard astronomical software such as IRAF, or by developing its own software.

In order to develop software to work with the FITS format is needed to download and install the CFITSIO libraries form the NASA webpage: http://heasarc.gsfc.nasa.gov/fitsio/. The libraries are available in C and Fortran languages and basically consist of several subroutines that executes different tasks such as reading and creating FITS type files. The subroutines are named with a 'letter code' that indicates the type of task that they are able to perform as well as the data type of its associated parameters. This information as well as a brief description of the CFITSIO libraries is available to download also in the NASA webpage cited before, in the documents called 'C/Fortran Programmers Reference Guide'.

The reading and writing of a FITS type file mainly consists in to access the information (value) of each image pixel without loosing its position in the image information by a bi-dimensional array. This means that the basic parameters of the image are the two spatial coordinates of each pixel and its associated value. Extra information could be stored and read from a header (For example: Observation information and history processing of the image)

For example, in order to read or write a FITS type file, we always need to follow the same logical procedure, opening the file, determining the size of the image, reading/writing

and closing. For those purposes we are able to use several routines. The names of the routines of the CFITSIO libraries allways start with the letters 'ft', but the routines that read information from a file starts with the letters 'ftg', however the ones that writes information in a file starts with the letters 'ftp'. The data type of the information stored in the images is given by the last letter of the routine names. the letter code is the following:

x-bit

b - character*1 (unsigned byte)

i - short integer (I*2)

j - integer (I*4, 32-bit integer)

k - long long integer (I*8, 64-bit integer)

e - real exponential floating point (R*4)

f - real fixed-format floating point (R*4)

d - double precision real floating-point (R*8)

g - double precision fixed-format floating point (R*8)

c - complex reals (pairs of R*4 values)

m - double precision complex (pairs of R*8 values)

l - logical (L*4)

s - character string

That is the way to quickly identify the kind of routine that we are looking for to do the required job in the libraries subroutines list. The names of the subroutines should not be changed.

The usage of this libraries has many applications in the astronomical studies, because it allows to transform a FITS type image into a different type of image or text file, and viceversa. Which is a very usefull tool if working with several data types and for instance with different observational reduction software.

REFERENCES

9. Bibliografía

Abraham, R. G., Merrifield, M. R., Ellis, R. S., Tanvir, N. R., & Brinchmann, J. 1999, MNRAS, 308, 569

Agertz, O., Teyssier, R., & Moore, B. 2009, MNRAS, 397, L64

Athanassoula, E. 1992, MNRAS, 259, 345

Barazza, F. D., et al. 2009, A&A, 497, 713

Barnes, E. I., & Sellwood, J. A. 2003, AJ, 125, 1164

Begeman, K. G. 1989, A&A, 223, 47

Bell, E. F., & de Jong, R. S. 2001, ApJ, 550, 212

Bissantz, N., Englmaier, P., & Gerhard, O. 2003, MNRAS, 340, 949

Blumenthal, G. R., Faber, S. M., Flores, R., & Primack, J. R. 1986, ApJ, 301, 27

Bottema, R. 1993, A&A, 275, 16

Bournaud, F., & Elmegreen, B. G. 2009, ApJ, 694, L158

Buta, R., & Block, D. L. 2001, ApJ, 550, 243

Bruzual A., G., & Charlot, S. 1993, ApJ, 405, 538

Colín, P., Valenzuela, O., & Klypin, A. 2006, ApJ, 644, 687

Daigle, O., Carignan, C., Hernandez, O., Chemin, L., & Amram, P. 2006, MNRAS, 368, 1016

Debattista, V. P., Carollo, C. M., Mayer, L., & Moore, B. 2004, ApJ, 604, L93

Dekel, A., & Birnboim, Y. 2006, MNRAS, 368, 2

Dekel, A., Sari, R.,

Dekel, A., Sari, R., & Ceverino, D. 2009, ApJ, 703, 785

Duval, M. F., & Athanassoula, E. 1983, A&A,121, 297

Eskridge, P. B., et al. 2000, AJ, 119, 536

Li, C., Gadotti, D. A., Mao, S., & Kauffmann, G. 2009, arXiv:0902.1175

Gabbasov, R. F., Repetto, P., & Rosado, M. 2009, ApJ, 702, 392

García-Barreto, J. A., Hernández-Toledo, H., Moreno-Díaz, E., Bernal-Marín, T., & Villarreal-Castillo, A. L. 2007, AJ, 134, 142

García-Barreto, J. A., Carrillo, R., & Vera-Villamizar, N. 2003, AJ, 126, 1707

García-Barreto, J. A., & Rosado, M. 2001, AJ, 121, 2540

García-Barreto, J. A., Rudnick, L., Franco, J., & Martos, M. 1998, AJ, 116, 111

García-Barreto, J. A., Scoville, N. Z., Koda, J., & Sheth, K. 2005, AJ, 129, 125

Gnedin, O. Y., Kravtsov, A. V., Klypin, A. A., & Nagai, D. 2004, ApJ, 616, 16

Hernández-Toledo, H. M., Vázquez-Mata, J. A., Martínez-Vázquez, L. A., Avila Reese, V., Méndez-Hernández, H., Ortega-Esbrí, S., & Núñez, J. P. M. 2008, AJ, 136, 2115

Hernández-Toledo, H. M., Vázquez-Mata, J. A., Martínez-Vázquez, Changbom Park and Y.Y Choi. 2009, AJ, in press

Ho, L. C., Filippenko, A. V., & Sargent, W. L. W. 1997, ApJS, 112, 315

Hohl, F. 1978, AJ, 83, 768

Holley-Bockelmann, K., Weinberg, M., & Katz, N. 2005, MNRAS, 363, 991

Jedrzejewski, R. I. 1987, MNRAS, 226, 747

Kalnajs, A. J., & Athanassoula-Georgala, E. 1974, MNRAS, 168, 287

Laurikainen, E., Salo, H., Buta, R., & Knapen, J. H. 2007, MNRAS, 381, 401

Li, C., Gadotti, D. A., Mao, S., & Kauffmann, G. 2009, arXiv:0902.1175

Menéndez-Delmestre, K., Sheth, K., Schinnerer, E., Jarrett, T. H., & Scoville, N. Z. 2007, ApJ, 657, 790

Merritt, D., & Tremblay, B. 1994, AJ, 108, 514

Pérez, I., Fux, R., & Freeman, K. 2004, AAP, 424, 799

Rhee, G., Valenzuela, O., Klypin, A., Holtzman, J., & Moorthy, B. 2004, ApJ, 617, 1059

Rubin, V. C., Thonnard, N., & Ford, W. K., Jr. 1978, APJ, 225, L107

Sales, L. V., Navarro, J. F., Schaye, J., Dalla Vecchia, C., Springel, V., Haas, M. R., & Helmi, A. 2009, MNRAS, 399, L64

Sellwood, J. A. 2008, ApJ, 679, 379

Sheth, K., et al. 2008, ApJ, 675, 1141

Spekkens, Kristine; Giovanelli, Riccardo; Haynes, Martha P. 2005, AJ, 29.2119S

Spekkens, K., & Sellwood, J. A. 2007, APJ, 664, 204

Stanimirovic, S., Staveley-Smith, L., Dickey, J. M., Sault, R. J., & Snowden, S. L. 1999, MNRAS, 302, 417

Tremaine, S., & Weinberg, M. D. 1984, ApJ, 282, L5

Valenzuela, O., & Klypin, A. 2003, MNRAS, 345, 406

Valenzuela, O., Rhee, G., Klypin, A., Governato, F., Stinson, G., Quinn, T., & Wadsley, J. 2007, APJ, 657, 773

Veron-Cetty, M.-P., & Veron, P. 1986, A&AS, 66, 335

Weinberg, M. D., & Katz, N. 2007, MNRAS, 375, 460

Weiner, B. J., Sellwood, J. A., & Williams, T. B. 2001, APJ, 546, 931

Weiner, B. J., Williams, T. B., van Gorkom, J. H., & Sellwood, J. A. 2001, APJ, 546, 916

Wells, D. C., Greisen, E. W., & Harten, R. H. 1981, A&AS, 44, 363